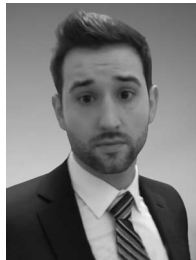


Numerical Investigation of Secondary Vortex Structures in a Rotor Wake



Andrew Bodling
Research Scientist
Science and Technology Corporation
Moffett Field, CA, USA



Mark Potsdam
Research Scientist
U.S. Army Combat Capabilities Development Command
Aviation & Missile Center, Moffett Field, CA, USA

In hovering rotor computational fluid dynamics simulations, a common phenomenon is the breakdown of the primary vortex system due to secondary vortices, which are characterized by S-shaped vortical structures appearing between the primary blade-tip vortices. Since the presence of the secondary vortices is strongly influenced by the numerical settings, the degree to which secondary vortices physically occur warrants investigation. Therefore, this study investigates how the numerical settings affect the development of secondary vortices in hover simulations using the rotating blade geometry from previous experiments, where the focus is on temporal convergence. The computed near-wake vortical flow field is qualitatively compared to the experimental results. The calculations are then used to elucidate the secondary vortex development process, where it is shown that the secondary vortices develop by the interaction of the vortex sheet with the primary vortex structure. A number of parametric studies are done on the rotating blade geometry to investigate how the numerical settings affect the secondary vortex development process. Although the focus is on understanding the impact of temporal convergence, the effect of the off-body grid structure, grid rotation, mesh resolution, numerical dissipation, and time-step scaling is also studied. In contrast to previous work, the resulting wake breakdown from using the different numerical settings is compared both qualitatively and quantitatively. For relatively high flow solver subiteration convergence, the off-body grid structure and grid rotation have little effect on the development of the secondary vortex structures. However, at low solver subiteration convergence, larger differences occur between the torus and no torus grid structures. A parametric sweep on subiterations shows that as the subiteration residual drop increases the vortex sheet is broken down less and, correspondingly, both the rotor performance data and peak number of secondary vortices converge. The analysis shows that when the subiteration convergence or grid resolution is not high enough, the vortex sheet and primary vortex are broken down, which disrupt the development process and leads to fewer secondary vortices. To better understand the rotating blade case, a separate vortex ring study is done to observe how vortex breakdown is influenced by off-body grid structure and different levels of subiteration convergence. In agreement with the rotating blade case, when all flow solvers are sufficiently converged, vortex breakdown is minimized and the solution to the rotating and stationary torus is identical.

Nomenclature

c	blade chord, m
c_{tip}	chord at the blade tip, m
c_{∞}	speed of sound, m/s
d_c	vortex core diameter, m
f	rotor frequency, Hz
H	rotor height above the ground plane, m
l	mesh reference length, m
M_{∞}	vortex ring convection speed, m/s
R	rotor radius, m

R_r	vortex ring radius, m
Q_{tip}	nondimensional Q-criterion of tip vortex
$Q_{\text{pos/neg}}$	nondimensional Q-criterion of the secondary vortex with positive/negative sense of rotation
Δt	computational time-step size, °
U_{∞}	free-stream velocity, m/s
u, v, w	x, y, z -components of velocity, m/s
V_h	hover-induced velocity, m/s
x/R	normalized distance along the x -axis (parallel to rotor axis)
y/R	normalized distance along the y -axis (spanwise at $\Psi = 270^{\circ}$)
y^+	nondimensional distance from the wall to the first mesh node
α	blade pitch angle
Ψ	blade azimuthal angle, °
Ψ_w	rotor wake age (= 0° when blade parallel with the y -axis), °
ω_n	vorticity unit vector

Presented at the VFS International 76th Annual Forum & Technology Display, Virginia Beach, VA, October 6–8, 2020. This is a work of the U.S. Government and is not subject to copyright protection in the U.S. Distribution Statement A – “Approved for public release; distribution is unlimited” PR20200265 July 17, 2020. Manuscript received August 2021; accepted April 2022.

$\omega_{n,x/y/z}$	x, y, z -components of vorticity unit vector
$\omega_{x/y/z}l/c_\infty$	x, y, z -components of nondimensional vorticity vector
$\omega_{\max}d_c/U_\infty$	nondimensional peak vorticity magnitude
$ \omega l/c_\infty$	nondimensional vorticity magnitude
STB	Shake the Box
OOM	order of magnitude

Introduction

One of the key aspects of modeling rotorcraft flows is accurately predicting the complex vortex system produced by the rotor. A hovering rotorcraft sheds vortices from the tip of the rotor to form a helical vortex system below the rotor. The wake of a rotor in hover was believed to consist of only a helical vortex system for many years. However, as high-order (less dissipative) methods and finer grids were used to resolve the wake, scientists began to see smaller secondary vortex structures that formed between the primary vortices. At first glance, these structures were believed to be purely numerical artifacts. They did not conform to the canonical wake structure seen in any experimental flow visualizations. However, across the literature these secondary vortex structures repeatedly came up in high-fidelity calculations (Refs. 1–4), suggesting that they might be physical. The question of whether the secondary vortex structures, termed “worms,” were indeed physical was left unanswered for many years.

Wolf et al. (Ref. 5) conducted an experiment with a model helicopter “Align T-Rex 800” that was rigidly mounted above a horizontal ground plate. The main rotor was equipped with two untwisted “Spinblades Black Belt 685” rotor blades, which had a radius of $R = 0.775$ m and a chord length of $c = 0.061$ m. The rotor blades were rotated at a frequency of $f = 20.83$ Hz in a clockwise direction. Two heights H above the ground plane were used, $H = 0.7R$ and $H = 1.0R$. Volumetric flow measurements were taken of the rotor wake using the Lagrangian particle tracking “Shake the Box” (STB) method introduced by Schanz et al. (Ref. 6). These measurements showed the presence of secondary vortex structures that connected the primary helical vortices.

For the first time ever, the experiments by Wolf et al. (Ref. 5) showed that the “worm” structures observed in high-fidelity simulations were indeed a physical phenomenon. However, many questions about the “worm” structures still remain. It is not clear at this time how much and how many of the “worm” structures are physical and how much is numerical. In many cases, they seem to overwhelm the dominant tip vortex wake structure. Also, it is not entirely clear how and why they occur. Hariharan et al. (Ref. 7) point out that the structures are classical in spatial shear-layer evolution and inviscid helical wake instability (Ref. 8), seen in both experiments and computation. However, numerical issues could prematurely trigger the instabilities and structures. Chaderjian and Buning (Ref. 4) explained the process as wake shear-layer entrainment and roll-up into the rotor tip vortices along with vortex stretching based on computational fluid dynamics (CFD) animated visualizations. Abras et al. (Refs. 1, 7, 9) investigated the computational inputs that might effect the presence of the secondary vortex structures in the wake of a rotor in hover; inputs include grid structure, grid motion, time-step size, subiteration count, and turbulence modeling. In the grid study, a stationary Cartesian off-body grid (no torus) as well as a rotating and stationary torus off-body grid was used with different grid densities to investigate how these grid topologies influence the physical flow features and presence of complete wake breakdown (i.e., entire helical vortex system engulfed by “worm” structures, termed vortex “soup”). In addition, a separate case used tip-vortex adaptive mesh refinement (AMR) to better resolve the tip vortices. Building on these studies, Abras and Hariharan (Ref. 10) used volume rendering techniques to better un-

derstand the physics behind the evolution of wake breakdown. Some of the key conclusions of the studies from Abras et al. (Refs. 1, 7, 9, 10) are summarized in the list below:

- 1) Diffusing either the braid or tip vortex strength reduced breakdown, and it is the interplay of these two components that results in vortex “soup.”
 - 2) A small rotating torus surrounding the blade region compromised the tip vortex strength and reduced breakdown.
 - 3) Tip-vortex AMR reduced wake breakdown since it did not target and resolve the wake sheet.
 - 4) A stationary torus off-body grid leads to wake breakdown, while a rotating torus off-body grid did not.
 - 5) A stationary Cartesian off-body grid leads to wake breakdown.
 - 6) The size of the rotating torus off-body grid did not effect the wake breakdown.
 - 7) Rotational-mode computations yielded a clean helical wake.
- Based on the work from Abras et al. (Refs. 1, 7, 9, 10), some of the hypotheses that exist are below:
- 1) When the wingtip vortex is not sufficiently resolved, the flow is stabilized due to the excessive dissipation and the “worms” are suppressed.
 - 2) The presence of “worms” could be numerical artifacts that arise due to the unsteady interpolation between the near and off-body grids and/or change in hole-cutting in the torus grids.
 - 3) The rotating torus adds extra dissipation due to rotation, and therefore, stabilizes the flow and leads to fewer “worms.”
 - 4) Subiteration convergence could be an important factor in the breakdown of the wake.

The idea of the last hypothesis is that within each time step if the residual of the Navier–Stokes equations is not driven down *enough* towards zero (termed the solver residual drop in this paper), an error could build up over time. This error buildup could affect the physical flow features and result in a different number of secondary vortices.

Previous studies related to temporal convergence (Refs. 1, 11) did not look in the fine detail of how the subiteration residual drop affected the fundamental mechanisms of the secondary vortex development process. For example, Abras et al. (Ref. 1) observed that the wake breakdown did not significantly change as the number of subiterations and time-step size was varied. This study, however, did not look closely into the actual resulting temporal convergence. Perhaps doubling the subiterations did not make a difference since the subiteration convergence may have stalled. Alternately, as mentioned in the review paper by Hariharan et al. (Ref. 7), the study from Abras et al. (Ref. 1) may have not pushed the boundaries on temporal convergence sufficiently to have an impact on the wake breakdown. In another study, Abras and Hariharan (Ref. 11) investigated the impact of deep temporal convergence on hover prediction using the results of a higher order stream-wise upwind/Petrov-Galerkin finite element method. Although related to temporal convergence, this study focused more on performance predictions rather than the secondary vortex development process.

The objective of this paper is to meticulously study how the numerical settings affect the development of secondary vortices in hover simulations using the rotating blade geometry from previous experiments (Ref. 5), where the focus is on temporal convergence. The computed near-wake vortical flow field is qualitatively compared to the experimental results. The calculations are then used to elucidate the secondary vortex development process. A number of parametric studies are then done on the rotating blade geometry to investigate how the numerical settings affect the secondary vortex development process. Although the focus is on understanding the impact of temporal convergence, the effect of the off-body grid structure, grid rotation, mesh resolution, numerical dissipation, and time-step scaling is also studied. In contrast to previous work, the resulting wake breakdown from using the different numerical settings is

compared both qualitatively and quantitatively. To better understand the rotating blade case, a separate vortex ring study is done to observe how vortex breakdown is influenced by off-body grid structure and different levels of subiteration convergence. The current effort helps draw conclusions on recommended grid resolution and temporal convergence and whether off-body grid structure impacts wake breakdown. This paper also describes the relationship between the rotor performance predictions, the number of secondary vortices, and the vortex sheet. Finally, this study helps better understand the results from Abras et al. (Refs. 1, 9), such as why the wake breakdown of the stationary and rotating torus differed significantly.

Numerical Methodology

For the simulations, Helios version 9.0 (Ref. 12) is used. Helios is the rotary-wing product of the U.S. Army and the HPCMP CREATE-AV (Air Vehicles) program sponsored by the DoD High-Performance Computing Modernization Office. Helios employs an innovative multimesh, multisolver paradigm for CFD that uses unstructured and/or structured meshes in the “near-body” surrounding the solid surfaces to capture the wall-bounded viscous effects. Several near-body solvers are available in the latest Helios release, including unstructured mesh NSU3D, FUN3D, and kCFD; curvilinear structured mesh OVERFLOW; and strand mesh mStrand. Cartesian grids are used in the “off-body” to resolve the wake through a combination of higher order algorithms and AMR. The Cartesian meshes are managed by a block-structured mesh system, which has the ability to accommodate the geometry and solution features. An overset procedure (PUNDIT) (Ref. 13) facilitates the data exchange and also enables the relative motion between moving meshes. A lightweight Python-based software integration framework orchestrates the simulation and data exchange between modules. The main Helios flow solver modules used in this study are now described.

Flow solvers

FUN3D

FUN3D 13.5 (Ref. 14) is a near-body unstructured grid flow solver that has been continuously developed and supported by NASA Langley. It is a node-centered, finite-volume unsteady Reynolds-averaged Navier-Stokes (URANS) solver. It is spatially second-order accurate using a Roe upwind scheme. Time-accurate computations utilize an optimized, second-order, backward difference (BDF2OPT) time stepping scheme along with dual time-stepping subiterations. The SA-DDES turbulence model with Dacles-Mariani rotation correction and negative turbulence variable provisions is used (Refs. 15–17).

OVERFLOW

The near-body solver OVERFLOW 2.2o (Ref. 18), a structured, curvilinear grid flow solver developed by NASA Langley, is a node-centered, finite-difference unsteady URANS solver. A nominally spatially fifth-order accurate central difference scheme with fourth-difference-based scalar artificial dissipation is chosen for this study. The amount of artificial dissipation is controlled by DIS4 the fourth-order dissipation coefficient and SMOO the smoothing parameter which changes how the spectral radius of the Jacobian matrix is computed. Based on previous numerical experiments, a value of DIS4 between 0.005 and 0.04 is recommended, where the DIS4 coefficient used should be kept as small as possible while still maintaining stability. With SMOO = 0.0, the spectral radius is computed as normally, $|U| + kc$. With SMOO = 1.0,

the sound speed c is replaced by the local velocity scaled by the reference Mach number $\|V\|/M_{ref}$, which reduces smoothing in low-speed regions. Intermediate values of SMOO combine the effects of both the speed of sound and local velocity. More information about these parameters, including the form of the artificial dissipation operator is given in Jespersen et al. (Ref. 19). Time-accurate computations utilize an optimized, second-order, backward difference (BDF2OPT) time-stepping scheme along with dual time-stepping subiterations. The SA-DDES turbulence model with Dacles-Mariani rotation correction is used (Ref. 20). Unless mentioned otherwise, a fourth-order dissipation coefficient of DIS4 = 0.04, a smoothing parameter of SMOO = 0.0, and a constant local Courant–Friedrichs–Lewy (CFL) number is applied.

SAMCART

The Cartesian solver SAMCART is used for the off-body mesh system (Refs. 21, 22). SAMCART solves the Euler or Navier–Stokes equations using a fifth-order accurate central difference spatial discretization scheme for the inviscid terms and fourth-order for the viscous terms. The solver uses an implicit second-order BDF2 LU-SGS time integration scheme. AMR can be used to accurately, efficiently, and automatically capture the features in unsteady flow based on suitable adaption criteria. User-defined rectangular regions of a particular grid resolution can also be input. This fixed refinement capability is used in the current effort in order to fully and uniformly capture the blade wake sheets and tip vortices. The SA-DES turbulence model with the Dacles-Mariani rotation correction is used.

Geometry Modeling, Meshing, and Boundary Conditions

The model helicopter “Align T-Rex 800” is simulated under the same flow conditions as in the experiment by Wolf et al. (5). A sketch of the test section and coordinate system is shown in Fig. 1. The helicopter is placed at a height above the ground of $H = 0.7R$ and $H = 1.0R$, which is referred to as configurations TC1 and TC2, respectively, in the experiment (5). The blade pitch angle $\alpha = -9.675^\circ$ was chosen to match the experiment. The boundary conditions at the helicopter fuselage and rotor blades are viscous adiabatic solid walls (i.e., no-slip wall with density/pressure extrapolation). Free-stream conditions are used at the far-field boundaries with an inviscid ground plane. The far-field boundaries are $15R$ away from the fuselage in each direction to avoid any boundary effects on the near-field solution. The coordinate system used by Wolf is duplicated here when compared with the experimental data. X is parallel to the rotor axis and points downward. Y is spanwise at $\Psi = 270^\circ$ azimuth (out the right side of the helicopter with a clockwise rotating rotor). Z is in the azimuthal direction in the direction of blade rotation. The coordinate system origin is at the blade tip when the blade is at $\Psi = 270^\circ$. The experiment includes a small amount of blade bending and coning, which the calculations do not account for. The STB measurement volume extends to the ground in the X direction, $0.1R$ inboard, and $0.3R$ outboard in Y from the blade tip, and approximately 12° in the azimuthal (Z -ish) direction.

Figures 2(a) and 3(a) show a top and side view of the meshes for the no torus case. The green mesh denotes the trimmed unstructured near-body volume mesh used to model the fuselage geometry, which is solved by FUN3D. This mesh has 2.6 M nodes. Throughout the entire fuselage grid, $y^+ < 1$. All FUN3D calculations use 10 subiterations, which ensures a 3 order of magnitude (OOM) subiteration residual drop or an absolute residual of 10 OOM at the final subiteration. The residual drop is computed from the L_2 -norm of the mean flow residual and is not volume scaled. The drop in residual within dual iterations is reported.

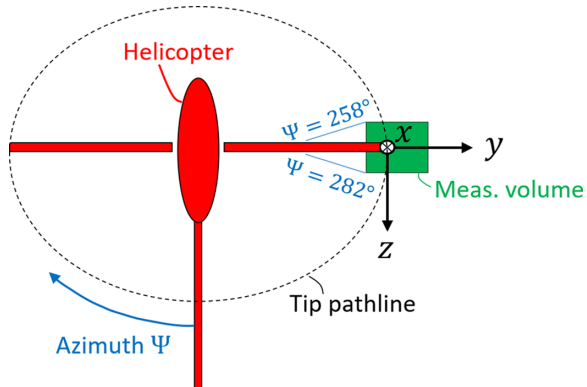
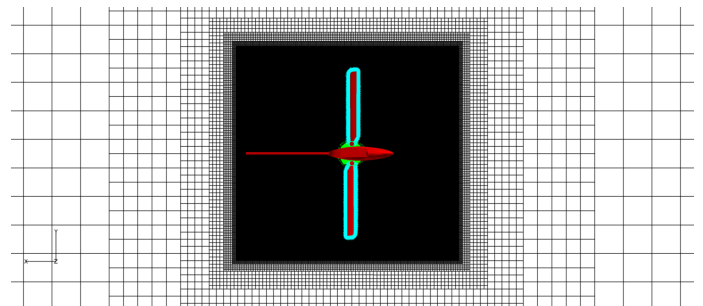


Fig. 1. Sketch of the test section geometry and coordinate system.

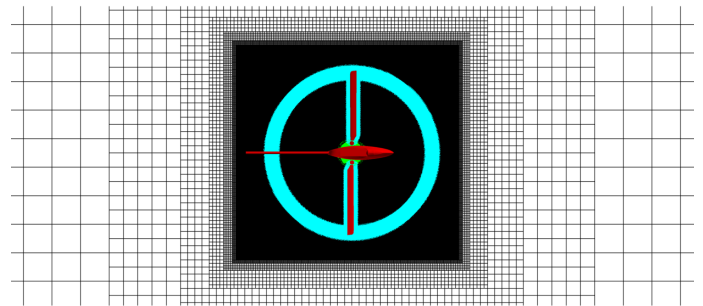
The blue mesh is the structured volume mesh that is used to model the rotor blades and is solved by OVERFLOW. The rotor blade grids consist of the overlapping main blade, root cap, and tip cap meshes. Each structured rotor blade mesh has 8.9 M points, with 7.4 M in the main blade; in the main blade there are 301, 243, and 101 points in the chordwise, spanwise, and normal direction, respectively. The blade volume meshes extend out 0.75 chords with an outer boundary spacing of 0.0015 m or $\sim 3.6\% c_{tip}$, where c_{tip} is the airfoil chord at the wingtip. For the majority of the blade grid, the $y^+ < 1$, except close to the leading edge where the y^+ is as large as 2.4 and the blade tip where the y^+ is as large as 4.4. Figures 2(b) and 3(b) show a top and side view with the structured torus mesh added. The torus mesh, colored in blue, is solved by OVERFLOW. It has a radial extent of 0.68–0.83 m (0.88–1.07R) and extends ± 0.075 m ($\pm 0.097R$) away from the blade tip in the vertical direction. The torus planar spacing is 0.0015 m ($\sim 3.6\% c_{tip}$) and has a total of 17.9 M grid points. All torus cases use a 0.2° azimuth spacing except the last section of this paper, which shows the effect of torus grid resolution, where a azimuth spacing of 1° is used. For the baseline calculations, which are compared to the experiment, using 50 OVERFLOW subiterations gives a subiteration residual drop of 1.25 OOM or an absolute residual of 4 OOM. The black mesh denotes the off-body Cartesian mesh that is solved by SAMCART. The wake is resolved with a single fixed refinement box with the finest resolution of $\Delta x = \Delta y = \Delta z = 5\% c_{tip}$. This fixed refinement box extends to the ground plane. In the last section of the paper, a coarser resolution of $\Delta x = \Delta y = \Delta z = 10\% c_{tip}$ is used to investigate the effect of off-body resolution on the development of the “worms.” Outside the fixed refinement box, the mesh is coarsened by a factor of two in all directions. Not including fringes, the finer off-body mesh has a total of 544 M grid points. Baseline calculations use 20 SAMCART subiterations, which gives a 2.4 OOM subiteration residual drop or an absolute residual of 4 OOM. For rotorcraft CFD applications, a subiteration residual drop of 2 OOM is often sufficient. This is an ad hoc rule that is widely used in practice. There are numerous successful CFD validation work on hover performance using this guideline (Refs. 4, 23, 24). Figure 4 shows the interface between the torus and Cartesian grids viewed from the top (Figs. 4(a) and 4(b)) and front (Fig. 4(c)). The front view shows that the Cartesian and torus mesh have a similar resolution in an azimuthal plane. The top views show that the $\Delta\Psi = 1.0^\circ$ torus mesh is coarser in the azimuth direction than the Cartesian mesh, while the $\Delta\Psi = 0.2^\circ$ torus mesh has similar spacing as the Cartesian mesh. A summary of the number of grid points for the main mesh components is shown in Table 1. All cases presented in this paper are run with a time-step size of $\Delta t = 0.25^\circ$, unless mentioned otherwise.

Table 1. Number of grid points for main mesh components (without fringes)

Volume Mesh	Number of Grid Points (M)
Fuselage	2.6
Total blade	8.9
Main blade	7.4
Torus, $\Delta\Psi = 0.2^\circ$	17.9
Cartesian, $\Delta x = 5\% c_{tip}$	544

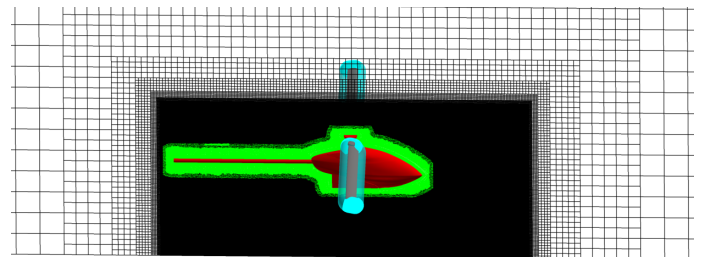


(a) No torus

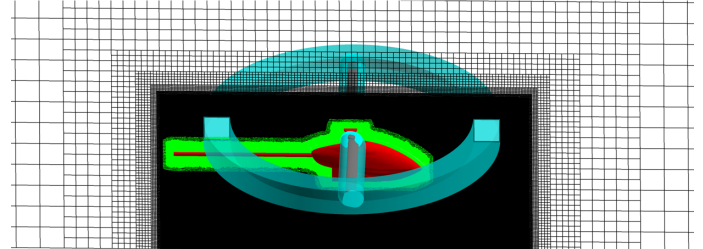


(b) Torus

Fig. 2. Top views of meshes for the (a) no torus and (b) rotating/stationary torus cases.



(a) No torus



(b) Torus

Fig. 3. Side views of meshes for the (a) no torus and (b) rotating/stationary torus cases.

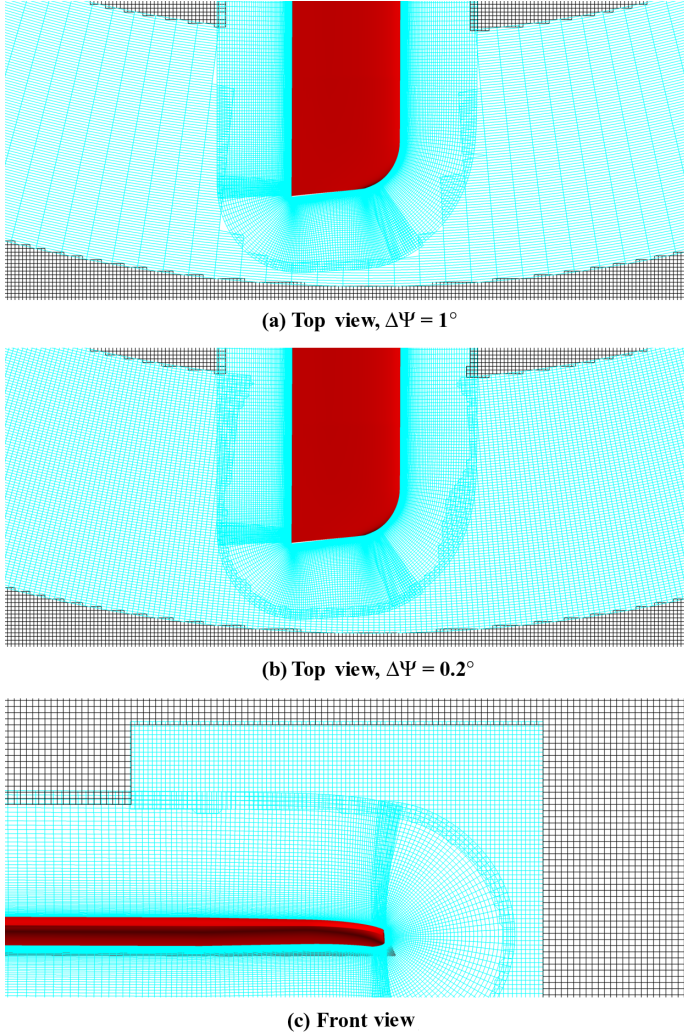


Fig. 4. (a) Top view $\Delta\Psi = 1^\circ$, (b) top view $\Delta\Psi = 0.2^\circ$, and (c) front view of the overlap between Cartesian and torus mesh.

Results

Comparison with experimental data

Each case is run sufficiently long to let any initial startup transients die out. After 10 revolutions, the figure of merit for each case changed by less than 0.1%. All snapshots and time-averaging shown in the paper are after 16 revolutions, which is several revolutions after the integrated forces have become statistically stationary. The experimental results were time-averaged over 3800 flow fields, corresponding to approximately 44 rotor revolutions. The simulation data were sampled every time-step (or every 0.25°) and time-averaged over a duration of two rotor revolutions. While this is a much shorter time duration than the experiment, the results did not significantly change when increasing the averaging duration from one to two rotor revolutions.

The experimental comparisons are done with the TC1 configuration using the no torus case. Figure 5 shows a comparison of the time-averaged velocity components from the current predictions and the experimental data from Wolf et al. (Ref. 5). Velocity profiles normalized by the hover-induced velocity V_h were taken along the radial direction at a constant $x/R = 0.35$, which is midway between the rotor and ground plane. The y -direction points outboard, and $y/R = 0$ is at the blade tip.

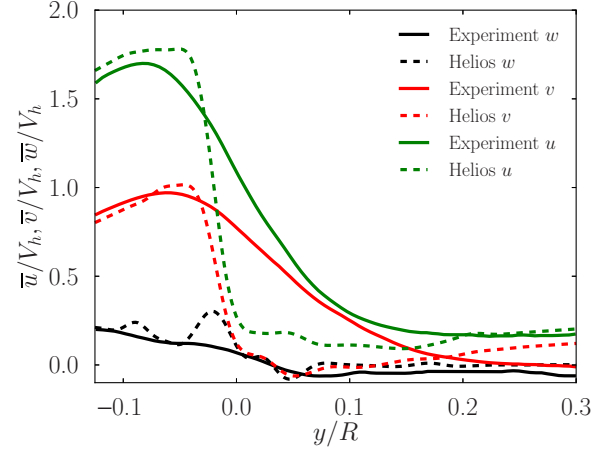


Fig. 5. Experimental (Ref. 5) and simulation comparison of velocity components in the wake along the radial direction at a constant $x/R = 0.35$. Velocity is normalized by the hover-induced velocity V_h .

Experimental data are shown in solid lines, while the predictions are shown in dashed lines, with each component shown in a different color. The measured and predicted velocity components agree well except from $0.0 < y/R < 0.1$. In the experiment, the wake boundary is smeared a lot while in the predictions it is quite distinct. This could be due to wandering vortices in the experiment due to the large aperiodicity in the primary vortices, which were partly involved in vortex pairing processes (Ref. 5). The aperiodicity in the experiment arises from external disturbances, such as the disturbances from the tail rotor and swashplate, which are not present in the simulation.

As in the experiment from Wolf et al. (5), the unit vector can be used to decompose the Q-criterion into Cartesian components (Ref. 25), for the experimental STB measurement volume. The vorticity unit vector $\vec{\omega}_n$ is defined as

$$\vec{\omega}_n = (\omega_{n,x}, \omega_{n,y}, \omega_{n,z}) = \frac{\nabla \times \vec{u}}{|\nabla \times \vec{u}|}. \quad (1)$$

Using the unit vector components, the tip vortices are identified as

$$Q_{\text{tip}} = \begin{cases} \omega_{n,z} \cdot Q, & \text{if } \omega_z l/c_\infty \geq 1.6 \\ 0, & \text{if } \omega_z l/c_\infty < 1.6, \end{cases}$$

where $\omega_z l/c_\infty$ is z -vorticity ω_z normalized by the mesh reference length l and speed of sound c_∞ . For the secondary vortices, the Q-values are multiplied with a projection of the unit vorticity vector onto the x, y -plane:

$$\omega_{n,xy} = \sqrt{\omega_{n,x}^2 + \omega_{n,y}^2}. \quad (2)$$

This accounts for the oblique S-shape of the secondary vortex structures. The positive and negative sense of rotation of the secondary vortices are defined on the sign of the ω_x component where

$$Q_{\text{pos}} = \begin{cases} \omega_{n,xy} \cdot Q, & \text{if } \omega_x l/c_\infty \geq 0.5 \\ 0, & \text{if } \omega_x l/c_\infty < 0.5 \end{cases}$$

$$Q_{\text{neg}} = \begin{cases} \omega_{n,xy} \cdot Q, & \text{if } \omega_x l/c_\infty \leq -0.5 \\ 0, & \text{if } \omega_x l/c_\infty > -0.5 \end{cases}$$

The thresholds of 0.5 and 1.6 were chosen so that noise in the solution field was minimized. Figures 6 and 7 show an isometric view of the pre-

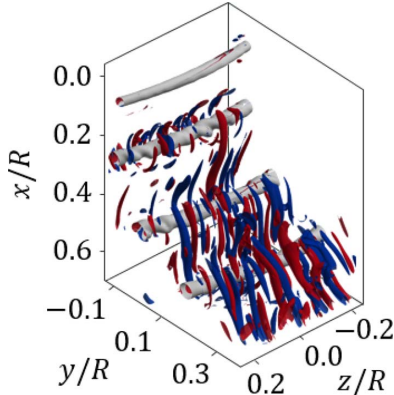


Fig. 6. Isometric view of the predicted instantaneous Q-isosurfaces from the TC1 no torus case at $\Psi_w = 70^\circ$. Q_{tip} is colored in gray, Q_{pos} is colored in red, and Q_{neg} is colored in blue. This color scheme is used in the remaining figures.

dicted and measured (Ref. 5) instantaneous Q-isosurfaces, respectively, at rotor wake age $\Psi_w = 70^\circ$; the corresponding side views are shown in Figs. 8 and 9. To show the aperiodicity of the measurements, the measured instantaneous Q-isosurfaces from Wolf et al. (Ref. 5) are shown at different rotor revolutions at the same wake age of $\Psi_w = 70^\circ$. Ψ_w is defined so that $\Psi_w = 0^\circ$ corresponds to when the blade is parallel with the y-axis. Q_{tip} is colored in gray, Q_{pos} is colored in red and Q_{neg} is colored in blue. The Q-values for the vortices are Q_{pos} and $Q_{neg} > 0.147$, and $Q_{tip} > 0.104$. There are several similarities between the measurements and predictions. In both cases, there is a mix of positive and negative rotating secondary vortices. The width of the secondary vortices is similar in the experiment and simulation. In both the experiment and simulation, the secondary vortices attach to the nearby primary vortices. In the predictions, however, there are more secondary vortices at the older wake ages than in the experiment. Note though that in the experiment, a geometric aspect ratio constraint was imposed with a minimum height of $\Delta x/R = 0.15$ and a maximum width of $\Delta z/R = 0.08$. This constraint was not imposed in the postprocessing of the simulation and, therefore, additional smaller structures are observed in the simulation that may have been present in the experiment.

Figure 10 shows the measured (top) and predicted (bottom) tip vortex strength Q_{tip} (gray) and negative secondary vortex strength Q_{neg} (blue) with rotor wake ages spanning from $\Psi_w = 5^\circ$ to $\Psi_w = 165^\circ$. Measured data are from Wolf et al. (Ref. 5). Measured data are averaged along the z-direction and in phase bins of $\Delta\Psi_w = 10^\circ$ (Ref. 5). Predicted data are

the instantaneous solution ($Q_{neg} > 0.147$) at a rotor wake age that is at the center of the phase bins used in the experiment; simulation data are not averaged along the z-direction. In the experiment, a secondary vortex appears at $\Psi_w = 75^\circ$ while in the simulation it appears a little earlier at $\Psi_w = 65^\circ$. In both the simulation and experiment, as the wake age increases the size of the secondary vortex increases and at $\Psi_w = 165^\circ$ it connects with the two adjacent primary vortices.

Since the Q-isosurfaces, by definition, do not show the shear layer, more insight into the secondary vortex evolution process can be gained by instead looking at the vorticity magnitude isosurfaces. Figure 11 shows the cross-sectional view of the predicted vorticity magnitude isosurfaces ($|\omega|l/c_\infty = 0.5$) at the key stages of the evolution process, $\Psi_w = 5^\circ, 75^\circ, 115^\circ$, and 165° . Isosurfaces are colored by vertical velocity u . All the remaining figures in this paper use the same isosurface value and color scheme. At $\Psi_w = 5^\circ$, the vortex sheet shed from the blade starts to wrap around the nearby primary vortex. At $\Psi_w = 75^\circ$ and 115° , the vortex sheet has wrapped around the nearby primary vortex. When it wraps around the primary vortex, it breaks apart into small coherent structures. The small coherent structures that are wrapped around the primary vortex are seen more clearly in the Q-isosurfaces shown previously in Fig. 6 (see the second primary vortex). At the same time, the vortex sheet is convecting downwards towards the next primary vortex. At $\Psi_w = 165^\circ$, the vortex sheet is entrained into the next primary vortex, similar to a classic mixing mechanism in shear layers (Ref. 4). This causes the vortex sheet to break apart into elongated s-shaped coherent structures, which are termed “worms.”

Effect of the off-body grid structure

Now that the secondary vortex development process has been elucidated, this section investigates how different simulation parameters, off-body grid structures, and grid rotation affects the development process. In this analysis, to minimize the ground effects, the TC2 configuration is used instead, which has a height $H = 1.0R$. Figure 12 shows a comparison of the rotating torus, stationary torus, and no-torus vorticity magnitude isosurfaces. All three cases have a SAMCART subiteration residual drop of 2.4 OOM and an OVERFLOW subiteration residual drop of at least 1.25 OOM. The rod pointing to the left in the full view is the tail boom of the model helicopter, while the contour in the center of the cross-sectional view is the fuselage. Comparing the wake breakdown of the three different simulations, all cases are very similar, especially the no torus and stationary torus cases. In particular, in all cases the location of where the secondary vortices start to develop is similar as well as their presence between all primary vortex structures. The main

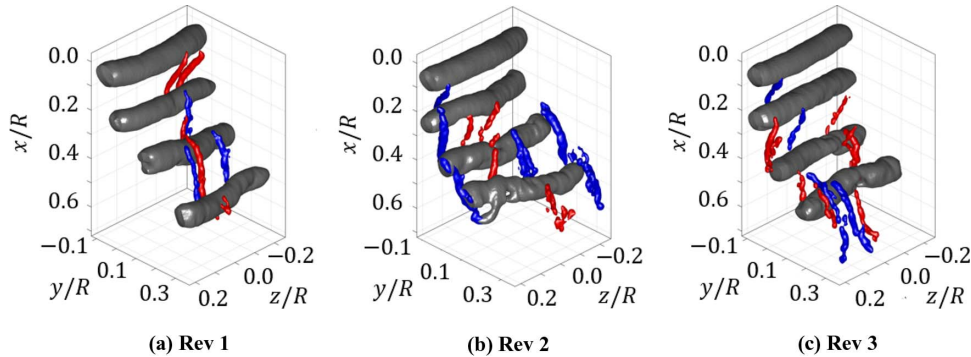


Fig. 7. Measured instantaneous Q-isosurfaces at different rotor revolutions from Wolf et al. (Ref. 5). All rotor revolutions are at the same wake age of $\Psi_w = 70^\circ$.

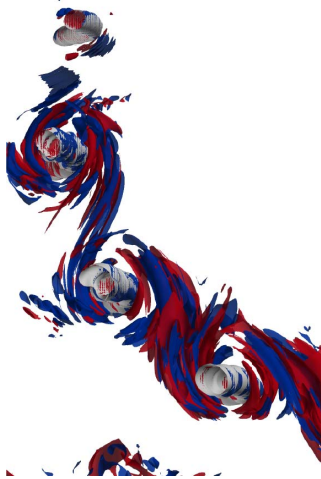


Fig. 8. Side-view of the predicted instantaneous Q-isosurfaces from the $H = 0.7R$ no torus case at $\Psi_w = 70^\circ$.

difference is the size of the secondary vortices, where the no torus case has finer-scale secondary vortex structures than the stationary torus and the stationary torus has finer-scale structures than the rotating torus. In the stationary torus, the moving overset boundary due to the blades may act as a numerical noise generator, which could lead to finer scale secondary vortices in the stationary torus case than the rotating torus. The finer-scale secondary vortices observed in the stationary torus case could also be due to the rotating torus being slightly more dissipative, which will be suggested later in the paper. Further research is necessary to fully understand this phenomenon.

Effect of subiteration convergence

Abras et al. (Ref. 1) found in their computations that the stationary torus lead to a complete breakdown of the wake while the rotating torus had a relatively clean wake. This is in contrast to the previous section,

where both the stationary and rotating torus leads to the breakdown of the wake. To better understand this, the effect of subiteration convergence is studied. To do this, a canonical problem using a three-dimensional vortex ring is studied to see how subiteration convergence effects the evolution of the vortex ring and how the evolution changes with a rotating/stationary torus.

The setup and initial solution of the vortex ring problem are shown in Fig. 13. The solution was initialized using a regularized form of the Biot-Savart law as described in Ref. 26. Points along the vertical red line are extracted over time to analyze how the peak vorticity changes as the ring translates downward. The analysis is done in Helios, using OVERFLOW for the torus grid and SAMCART for the off-body grid, as was done for the rotating blade case. The same flow conditions, grid resolution, and grid rotation rate as the rotating blade case is used. This makes the simulation very similar to the rotating blade case, except the helical vortex ring is initialized instead of generated by the rotating blade. The vortex core diameter $d_c = 0.00762$ m and the vortex ring radius $R_r = 0.755$ m. The height of the torus is $10d_c$. The vortex ring is initialized at the center of the torus. The self-induced convection speed of the vortex ring is $M_\infty = 0.1$. For the convergence study, the following cases are studied:

1. use $\Delta t = 0.25^\circ$ and 10 SAMCART subiterations while varying OVERFLOW subiterations,
2. use $\Delta t = 0.25^\circ$ and 50 OVERFLOW subiterations while varying SAMCART subiterations,
3. use 50 OVERFLOW subiterations and 10 SAMCART subiterations while varying the time-step size.

Vortex ring: Variation of OVERFLOW subiterations. Figure 14 shows the variation in the nondimensional peak vorticity magnitude $\omega_{\max} d_c / U_\infty$ of the two torus cases as a function of the peak vorticity location z/d_c . The vertical dashed line represents the interface between the torus (solved by OVERFLOW) and Cartesian (solved by SAMCART) grid. These plots are used to observe the change in vortex breakdown; a line that is smooth and reaches $z/d_c = 25$ represents a vortex that has not broken down (still has its circular shape). A line that is shifted downwards but is still smooth represents a vortex that has been dissipated but not broken

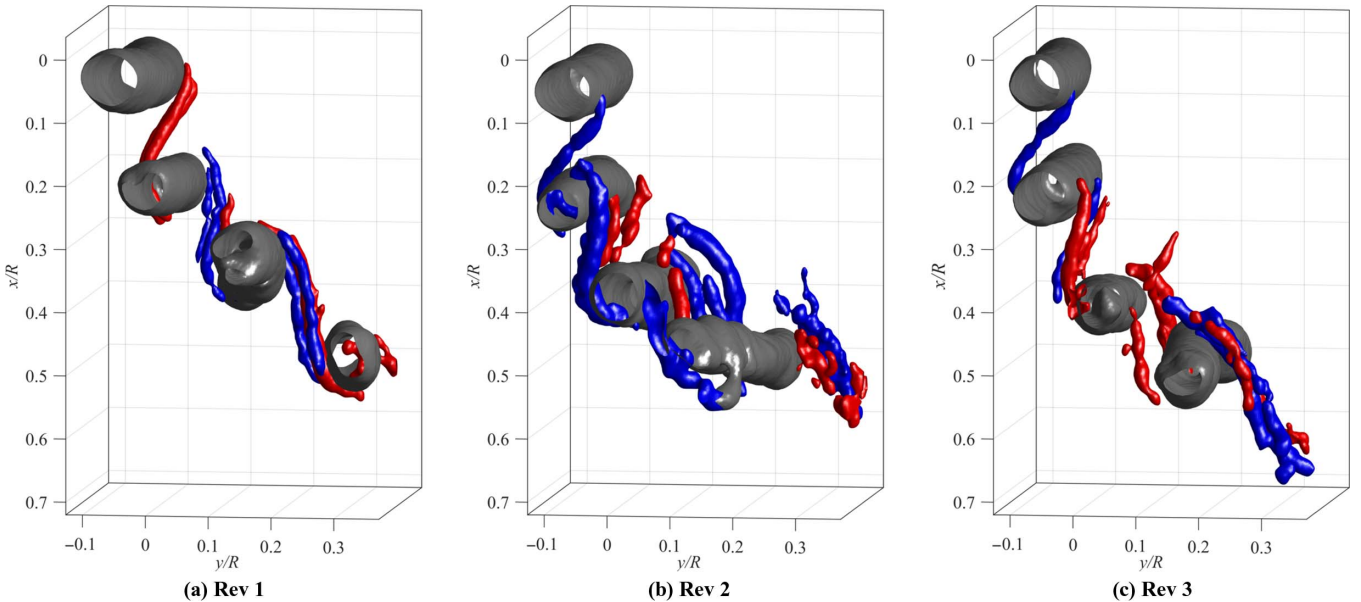


Fig. 9. Side view of measured instantaneous Q-isosurfaces at different rotor revolutions from Wolf et al. (Ref. 5). All rotor revolutions are at the same wake age of $\Psi_w = 70^\circ$.

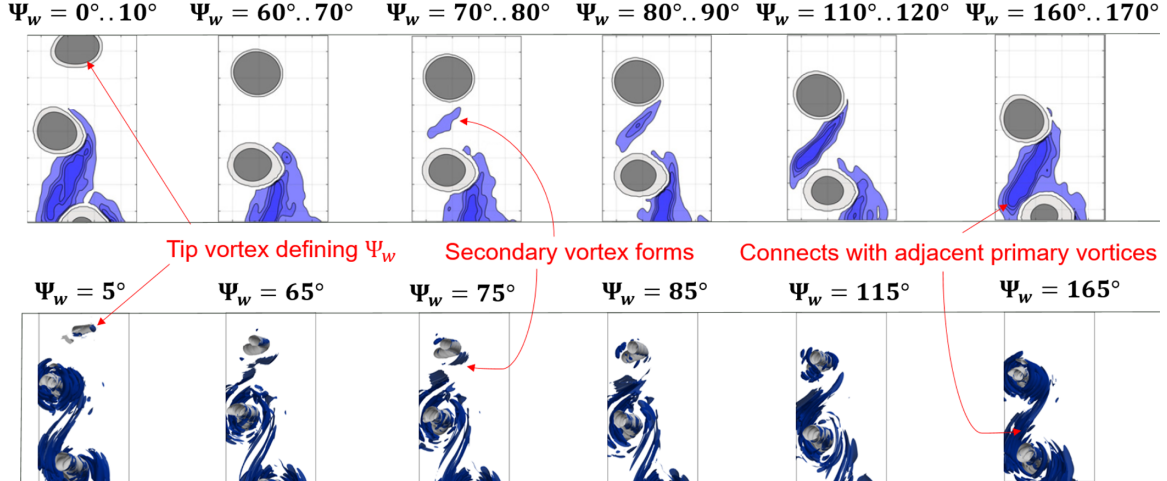


Fig. 10. Measured (top) and predicted (bottom) tip vortex strength Q_{tip} (gray) and negative secondary vortex strength Q_{neg} (blue). Measured data are averaged along the z -direction and in phase bins of $\Delta\Psi_w = 10^\circ$. Predicted data are the instantaneous solution ($Q_{\text{neg}} > 0.147$) at a rotor wake age that is at the center of the phase bins used in the experiment. Measured data are from Wolf et al. (Ref. 5).

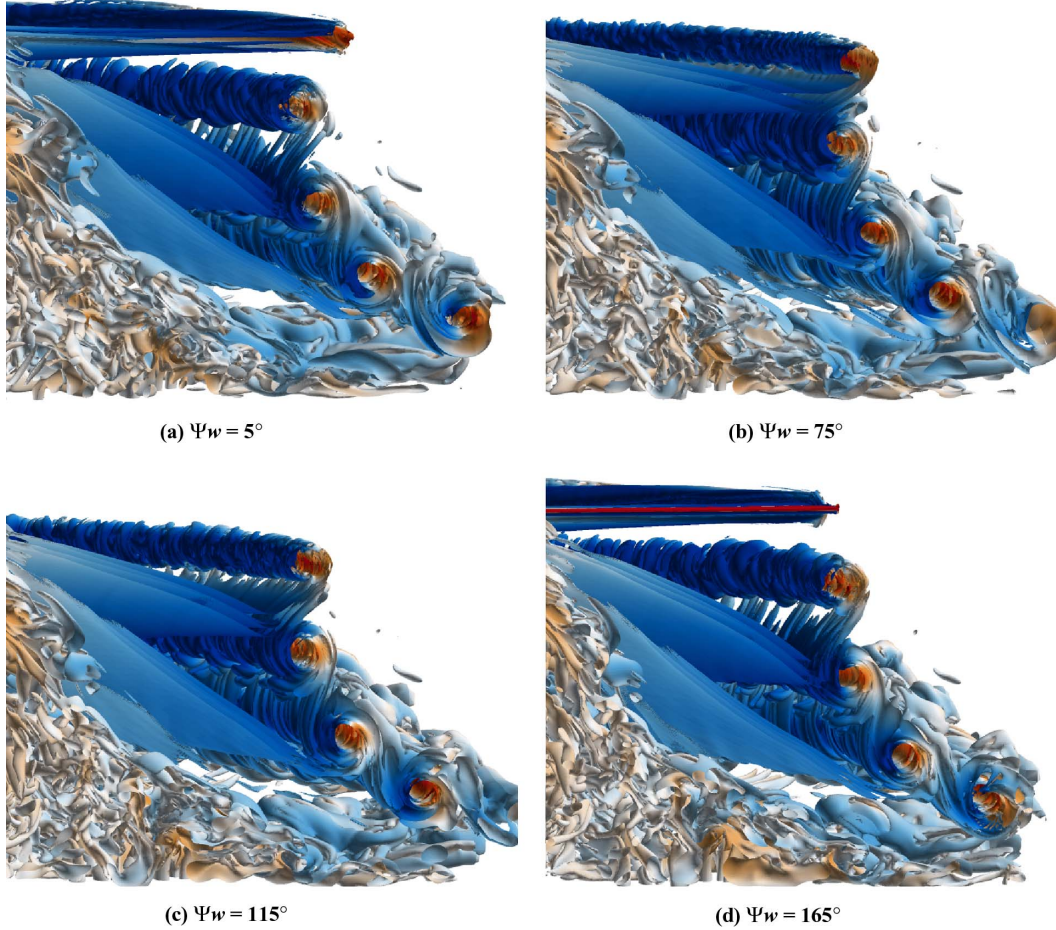


Fig. 11. Cross-sectional view of the vorticity magnitude isosurfaces ($|\omega|l/c_\infty = 0.5$) of the TC1 no torus case at (a) $\Psi_w = 5^\circ$, (b) $\Psi_w = 75^\circ$, (c) $\Psi_w = 115^\circ$, and (d) $\Psi_w = 165^\circ$.

down. All cases shown in the figure are with 10 SAMCART subiterations, which gives a global 1.00 OOM SAMCART residual drop. To clarify, this means that at a given time step, when SAMCART solves the Navier–Stokes equations, the residual drops by 1.00 order of magnitude

between the first and tenth subiteration. With five OVERFLOW subiterations (and a 0.33 OOM OVERFLOW residual drop), both the rotating and stationary torus vortex break down very quickly. Also, within the torus solution, the peak vorticity of the rotating torus is slightly smaller

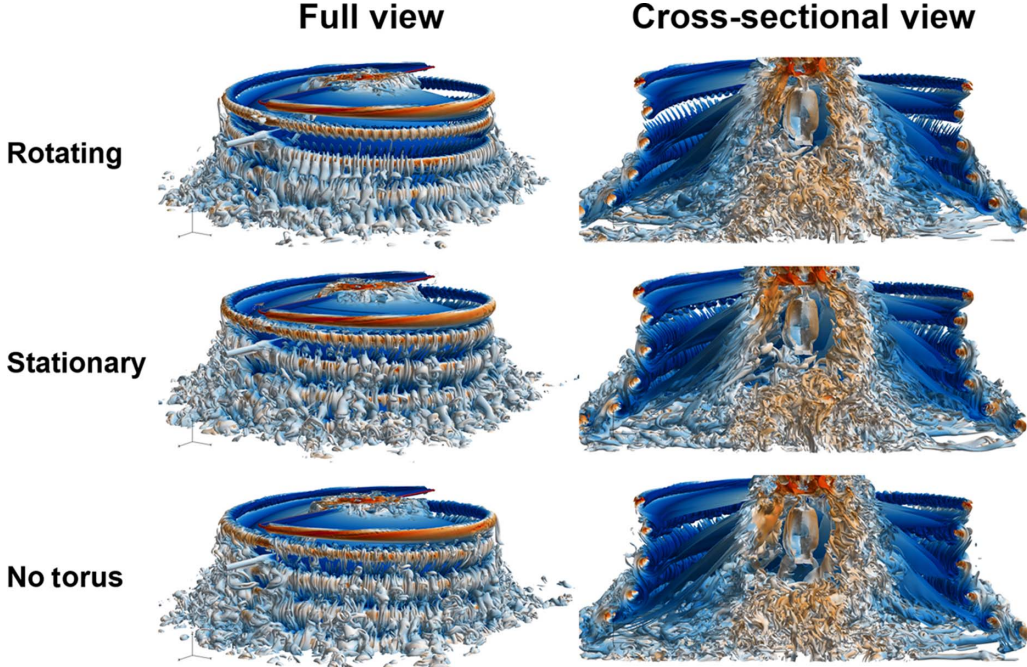


Fig. 12. Full and cross-sectional view comparison of the rotating torus, stationary torus, and no-torus vorticity magnitude isosurfaces. This figure and the remaining figures use the TC2 $H = 1.0R$ case.

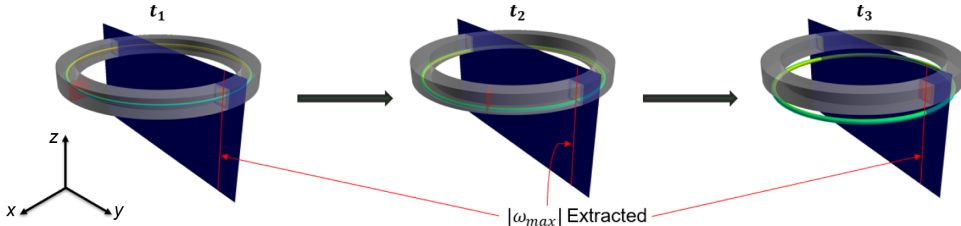


Fig. 13. Setup and initial solution (shown with vorticity magnitude isosurface) of the vortex ring problem. Points along the vertical red line are extracted over time to analyze how the peak vorticity changes as the ring translates downward.

than the stationary torus as visible in the zoomed region. However, at 25 subiterations (1.82 OOM OVERFLOW residual drop) the rotating and stationary torus solution within the torus is identical. This suggests that the rotating torus is slightly more dissipative than the stationary torus for low OVERFLOW convergence. Also, as more OVERFLOW subiterations are used (and OVERFLOW OOM residual drop increases), there is less vortex breakdown in the two cases. However, with using more than 50 subiterations (not shown) the solution in the entire flow domain no longer changes and vortex breakdown cannot be eliminated.

Vortex Ring: variation of SAMCART subiterations. Figure 15 shows the effect of SAMCART subiterations on vortex breakdown. All cases apply 50 OVERFLOW subiterations, which gives a 3.48 OOM OVERFLOW residual drop. Similar to the change in OVERFLOW subiterations, as the number of SAMCART subiterations increases, the vortex breakdown is less. However, with enough SAMCART subiterations (20), there is no longer any vortex breakdown and the solution for the two torus cases becomes nearly identical throughout the entire domain. Note that with additional SAMCART subiterations (not shown) the solution no longer changes. The conclusions drawn here are very important; it shows that when *all* flow solvers are sufficiently converged not only is the vortex breakdown minimized but the solution to the rotating and stationary torus is identical as well.

Vortex ring: Variation of time-step size. Figure 16 shows the effect of the time-step size on vortex breakdown. All cases used 50 OVERFLOW subiterations and 10 SAMCART subiterations. Similar to before, as the time-step size decreases (and the subiteration residual drop increases), vortex breakdown no longer occurs. In this case, it is not clear whether vortex breakdown is eliminated due to the increase in subiteration residual drop or the smaller time-discretization error. Therefore, several different time-step sizes were used, each with at least a 3.0 OOM OVERFLOW residual drop and a 2.0 OOM SAMCART residual drop (deemed to be sufficiently converged based on previous vortex ring simulations). The vortex breakdown for the different time-step sizes is shown in Fig. 17. As shown in the figure, there is no vortex breakdown for any time-step size, even with using a 1.0° time-step size. However, a smaller time-step size results in a less dissipated vortex. Therefore, it is clear that the subiteration residual drop affects the vortex breakdown while the time-step size affects the amplitude of the peak vorticity.

In Fig. 16, even with the simulation that applies a 0.125° time-step size, there exists a sudden drop in vorticity at the interface between the OVERFLOW and SAMCART grid. Sherer and Visbal (Ref. 27) performed multiresolution implicit large eddy simulations using a high-order overset grid approach applied to turbulent channel flow. In their study, they used different overset grid systems with sixth- and second-order interpolation schemes applied and compared the results to a single-

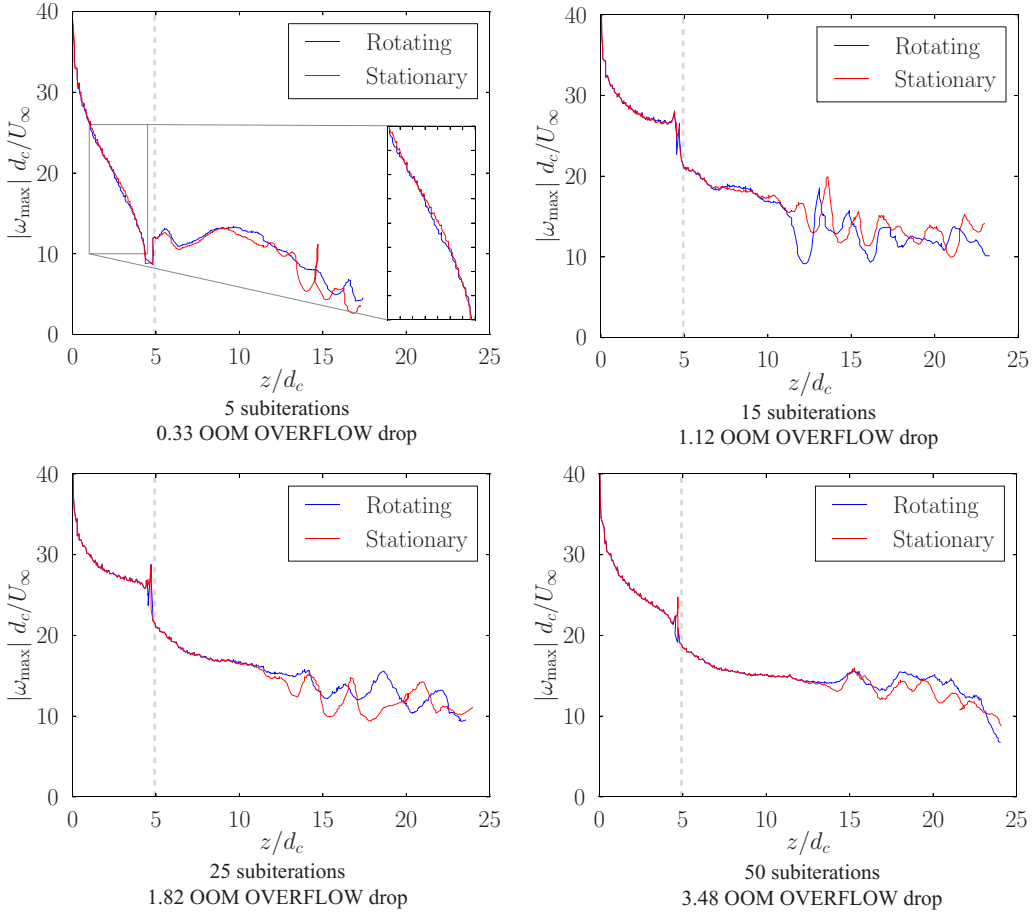


Fig. 14. Effect of OVERFLOW subiterations on vortex ring breakdown. All cases are with 10 SAMCART subiterations, which gives a global 1.00 OOM SAMCART residual drop. The vertical dashed line represents the interface between the torus and Cartesian grid.

grid case. Comparing the fluctuating velocity profiles of the sixth- and second-order interpolation schemes to the single-grid case, they found a large discrepancy in the profiles in the neighborhood of the grid interface when using standard second-order interpolation. This discrepancy is very similar to the one observed in the vortex ring simulations presented here. However, the use of sixth-order interpolation resulted in a smooth transition between grids that very closely matched the results from the single-grid case. Therefore, in the current simulations, the sudden drop in peak vorticity across the interface may be due to using second-order interpolation across the interface.

Rotating blade case: Variation in SAMCART subiteration convergence. In the following two sections, the rotating blade case is studied with different levels of flow solver subiteration convergence to observe the impact on wake breakdown. In the vortex ring case, varying the number of SAMCART subiterations influenced the peak vorticity profile in the off-body solution. Therefore, all three TC2 rotating blade cases are repeated with 10 instead of 20 SAMCART subiterations to see if changes in the peak vorticity profile downstream of the blades affect the development of the secondary vortices. The vorticity magnitude isosurfaces for the three different cases are shown in Fig. 18. The first and third columns are with 20 SAMCART subiterations applied (2.4 OOM SAMCART residual drop), and the second and fourth columns are with 10 SAMCART subiterations applied (1.2 OOM SAMCART residual drop). The areas to focus on for the discussion are denoted with the green oval.

Surprisingly, the number of secondary vortices is not affected much by the decrease in SAMCART subiteration convergence. Looking at the cross-sectional view in the last two columns, the vortex sheet and first primary vortex also do not change much. This relationship between the vortex sheet, primary vortex, and number of secondary vortices will be frequently observed in this paper.

Rotating blade case: Variation in OVERFLOW subiteration convergence. In the previous section, it was observed that when the vortex sheet and first primary vortex do not significantly change, the number of secondary vortices also does not significantly change. In this section, this trend is studied more as the OVERFLOW subiteration convergence is varied. To vary the OVERFLOW subiteration convergence, the time-step size is decreased from $\Delta t = 0.25^\circ$ to $\Delta t = 0.125^\circ$. Ten SAMCART subiterations are used for these and the remaining simulations in this paper. Decreasing the time-step size has an unexpected result on subiteration convergence; while it increases the SAMCART subiteration residual drop from 1.2 OOM to 1.8 OOM, it *decreases* the OVERFLOW global subiteration residual drop from 1.25 OOM to 0.68 OOM; the OVERFLOW global absolute residual also decreases from 4.47 OOM to 4.18 OOM. It is worth noting that looking at the *individual* grid components, with the smaller time-step size the torus absolute residual *increases* from 6.1 OOM to 6.47 OOM, while the main blade, root, and cap grids decrease in absolute residual. The reason for this peculiar convergence behavior is not clear, but the results still show us something very interesting. Figure 19 shows

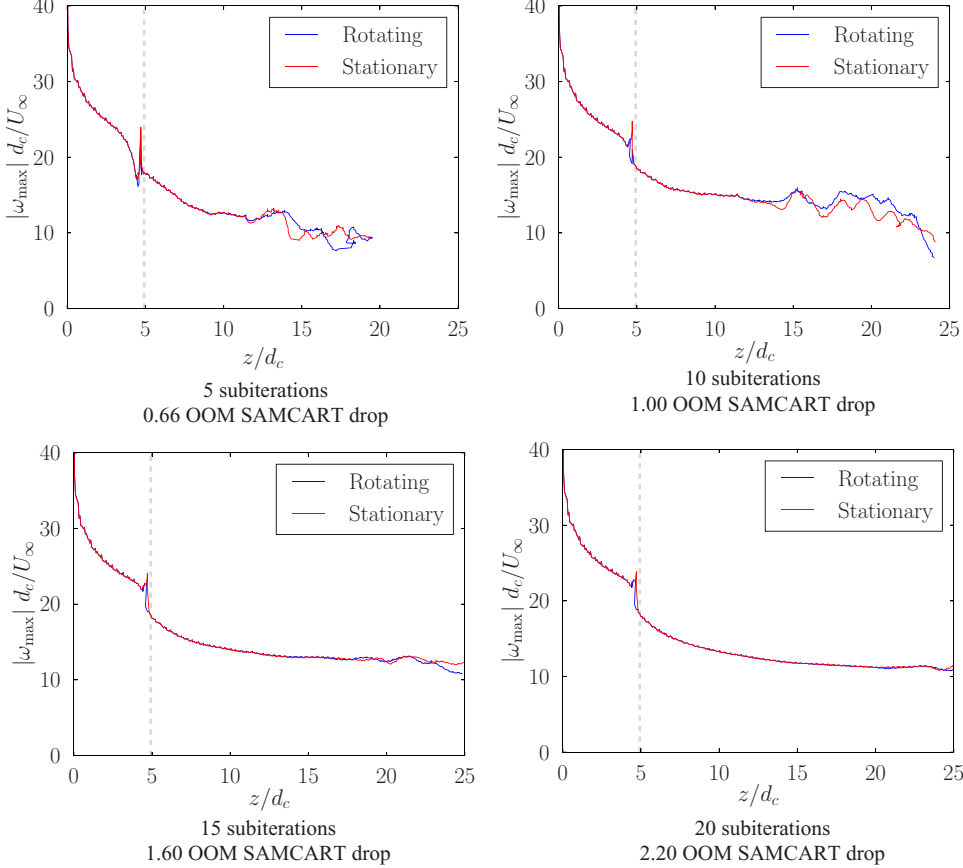


Fig. 15. Effect of SAMCART subiterations on vortex ring breakdown. All cases are with 50 OVERFLOW subiterations, which gives a global 3.48 OOM OVERFLOW residual drop.

a comparison of the three different rotating blade cases with the $\Delta t = 0.25^\circ$ case in the first and third columns and the $\Delta t = 0.125^\circ$ case in the second and fourth columns. The $\Delta t = 0.125^\circ$ case, with its lower OVERFLOW subiteration convergence, actually results in fewer secondary vortices, especially with the torus cases. Moreover, the vortex sheet with the two torus cases is significantly broken down and does not even connect with the first primary vortex. Also, especially with the rotating torus case, with lower OVERFLOW subiteration convergence there are much fewer secondary vortices wrapping around the first primary vortex.

Similar to the vortex ring case, a parametric sweep on OVERFLOW subiterations is performed using 2, 3, 5, 15, 25, 100, 150, and 250 OVERFLOW subiterations, which corresponds to a subiteration residual drop between 0.26 and 2.91 OOM. For the parametric sweep on OVERFLOW subiterations as well as the remaining simulations in the paper, a time-size of $\Delta t = 0.25^\circ$ is used. Figures 20 and 21 are the full and cross-sectional views of the stationary torus showing the impact on wake breakdown as OVERFLOW subiterations are varied. As seen in the cross-sectional views, the vortex sheet is broken down less as the subiterations (and subiteration convergence) increase. Above ~ 1.25 OOM residual drop, the vortex sheet no longer changes. This agrees with the vortex ring case discussed previously where above a certain subiteration convergence the vortex breakdown was minimal. Looking at the full views, as subiteration convergence increases there are fewer secondary vortices (especially from 0.26 to 0.77 OOM residual drop) until ~ 1.25 OOM residual drop where the secondary vortices appear to stop decreasing.

From the isosurfaces alone, it is not clear if the number of secondary vortices indeed converges above a residual drop of 1.25 OOM.

Therefore, the number of secondary vortices at different axial positions, ranging from $x/R = 0.1$ to $x/R = 0.8$, is quantified using the vortex identification scheme from Schwarz et al. (Ref. 28). For a given horizontal slice, the Q -criterion is applied to the velocity fields. Q is derived based on the assumption of a 2D velocity gradient tensor from the in-plane velocity components (v, w) according to Chen et al. (Ref. 29) by

$$Q = \frac{\partial v}{\partial y} \frac{\partial w}{\partial z} - \frac{\partial v}{\partial z} \frac{\partial w}{\partial y} - \frac{1}{2} \left(\frac{\partial v}{\partial y} + \frac{\partial w}{\partial z} \right)^2. \quad (3)$$

The Q -values are calculated based on velocity fields that are postprocessed using a 2D median filter with a size of 4.14 mm ($= 2\Delta y = 2\Delta z$) in both spatial directions to suppress noise. Only areas exceeding a threshold of $Q = 0.10$ are accepted while all lower values are set to zero. Additionally, the “bwpropfilt” function in MATLAB is used to only accept connected areas exceeding the Q -threshold that feature a minimum minor axis length of 4.14 mm. This approach was used in the joint experimental and numerical investigation by Schwarz et al. (Ref. 28) to quantify the development of secondary vortex structures in the wake of a two-bladed rotor out of ground effect. In that study, the number of secondary vortices detected in the experiment and simulation agreed well for axial positions $x/R \leq 0.6$.

For this analysis, data are sampled every four time steps (or every 1°) over a duration of five revolutions, resulting in 1800 velocity fields at each axial station. The data are analyzed in a radial band extending from $r = 0.68R$ to $r = 1.01R$. For a given axial position, the number of

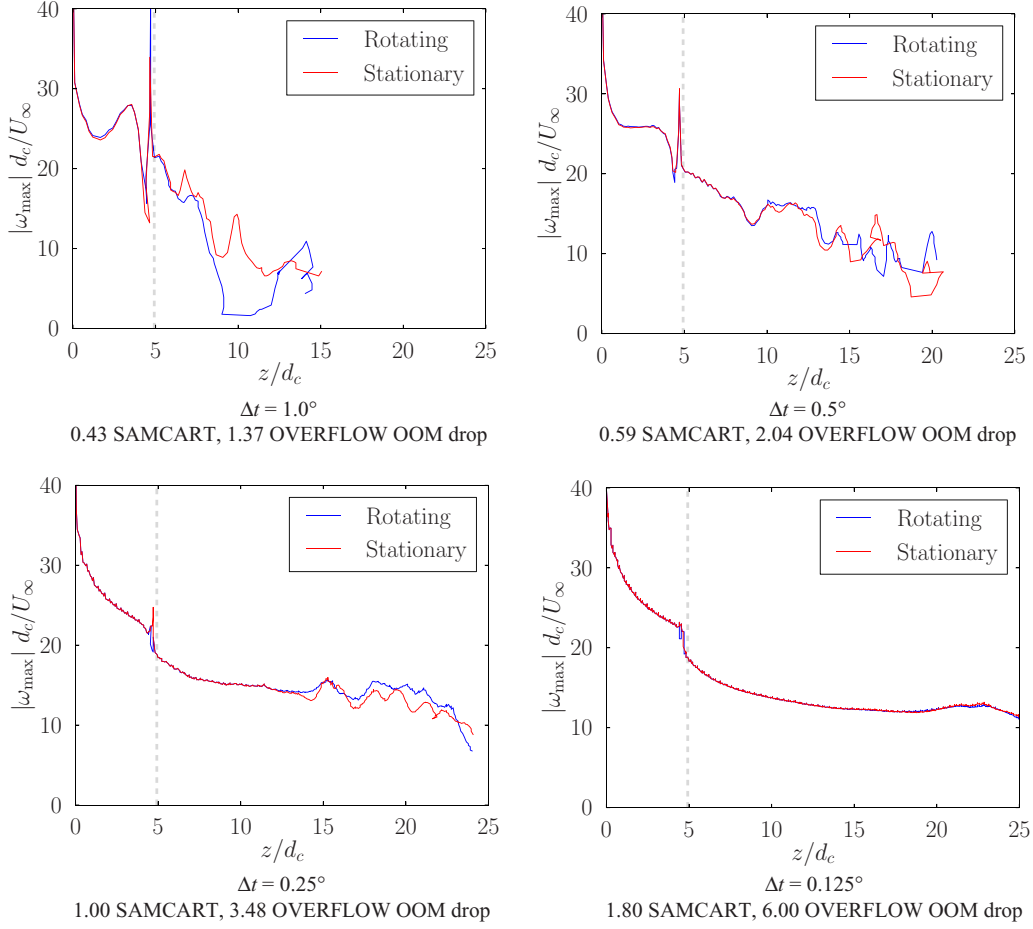


Fig. 16. Effect of time-step size on vortex ring breakdown. All cases are with 50 OVERFLOW subiterations and 10 SAMCART subiterations.

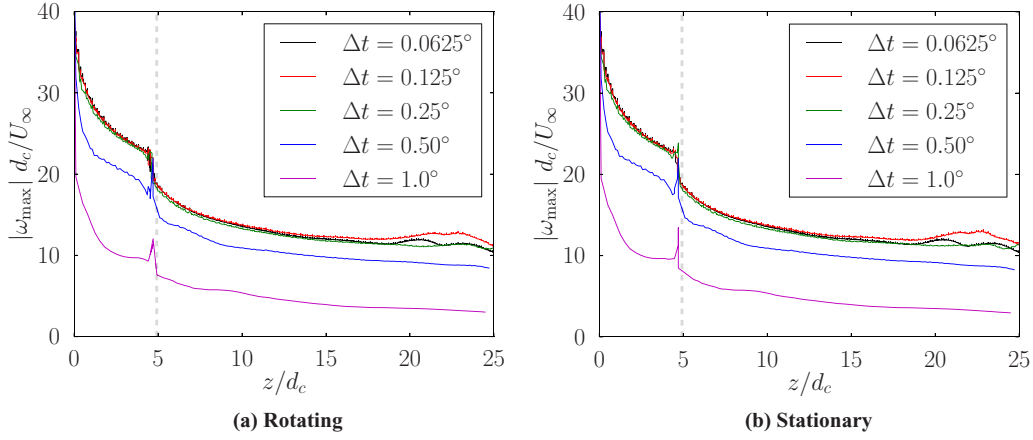


Fig. 17. Effect of changing time-step size on vortex ring breakdown for a sufficiently converged solution with the (a) rotating and (b) stationary torus.

secondary vortices in the radial band is computed at each time step. Then the average number of secondary vortices per time step for each axial position is found. Figure 22 shows the average number of secondary vortices per time step along the downstream direction for the parametric sweep on OVERFLOW subiterations. It is clear from the plot that as the subiteration convergence increases, the average number of secondary

vortices in each axial plane converges. Figure 23 shows a comparison of the peak number of secondary vortices (occurring at $x/R = 0.4$) and rotor performance data as the OVERFLOW subiteration residual drop increases. As the subiteration residual drop increases above 1.25 OOM, both the rotor performance data and peak number of secondary vortices converge. It was observed in Figs. 20 and 21 that above ~ 1.25 OOM

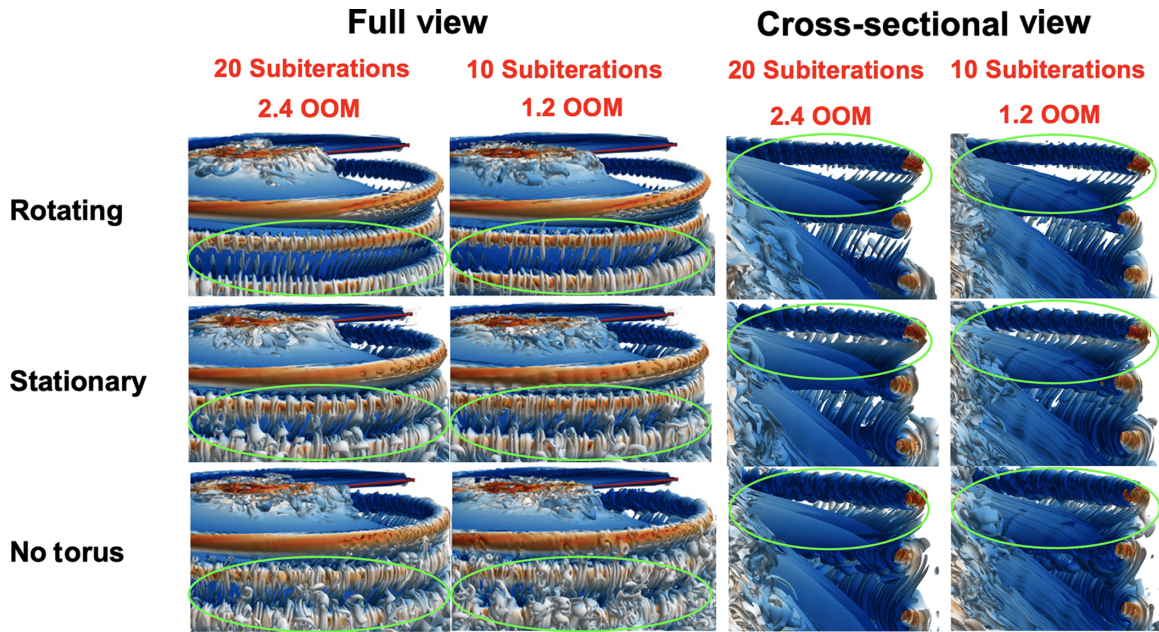


Fig. 18. Full and cross-sectional view showing the effect of SAMCART subiteration convergence on the development of secondary vortices. SAMCART subiteration convergence is decreased from 2.4 OOM to 1.2 OOM by decreasing the number of SAMCART subiterations from 20 to 10.

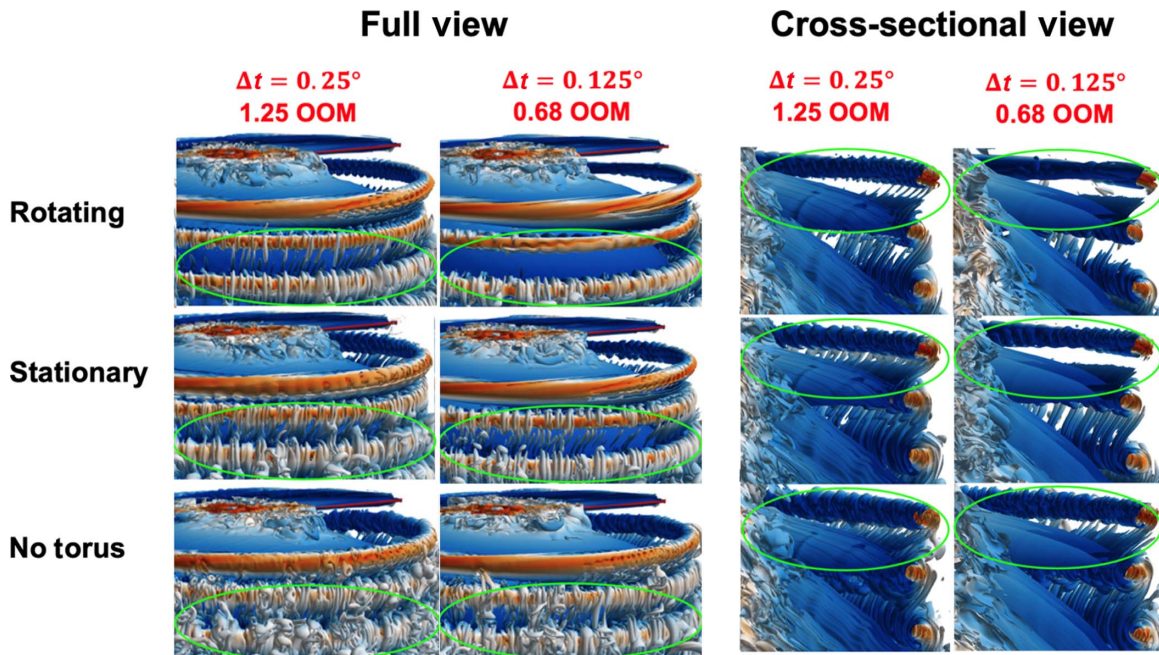


Fig. 19. Full and cross-sectional view showing the effect of time-step size on the development of secondary vortices. Time-step size is decreased from $\Delta t = 0.25^\circ$ (left column) to $\Delta t = 0.125^\circ$ (right column), which decreases the subiteration convergence from 1.25 OOM to 0.68 OOM.

residual drop, the vortex sheet no longer changes. This shows that when the secondary vortex development process is no longer disrupted by the breakdown of the vortex sheet, both the rotor performance predictions and the number of secondary vortices no longer change as well.

It was shown that for this particular flow solver and rotor configuration, the threshold for convergence of the wake breakdown is ~ 1.25 OOM. The last part of this section will observe the effect of changing the time-step scaling and numerical dissipation when the OVERFLOW

subiteration convergence is above this threshold (all simulations have above 1.4 OOM for all time steps). Figure 24 is a comparison of the average number of secondary vortices per time-step along the downstream distance using a constant CFL (used in previous simulations) and heuristic local time-step scaling based on the local volume. The figure shows that the number of secondary vortices does not change with the two different time-step scaling methods. This suggests that the particular time-step scaling method used may not have an impact on wake

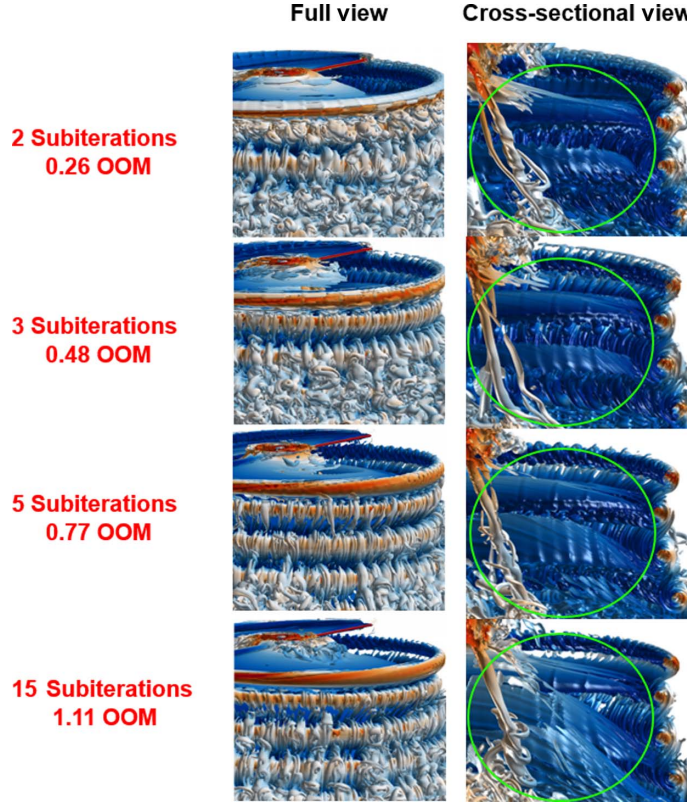


Fig. 20. Full and cross-sectional views of the stationary torus showing the impact on wake breakdown as OVERFLOW subiterations are varied using 2, 3, 5, and 15 OVERFLOW subiterations, which correspond to a subiteration residual drop between 0.26 and 1.11 OOM.

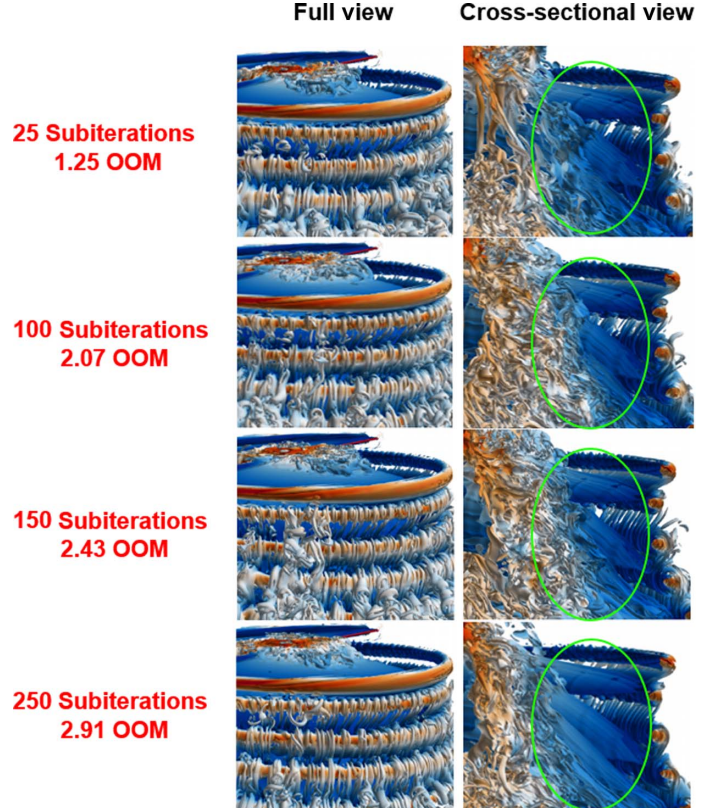


Fig. 21. Full and cross-sectional views of the stationary torus showing the impact on wake breakdown as OVERFLOW subiterations are varied using 25, 100, 150, and 250 OVERFLOW subiterations, which correspond to a subiteration residual drop between 1.25 and 2.91 OOM.

breakdown as long as the resulting subiteration residual drop is high enough. Figure 25 shows the variation in an average number of secondary vortices per time-step as numerical dissipation is varied by changing (a) numerical dissipation coefficient DIS4 and (b) smoothing parameter SMOO. Low, medium, and high numerical dissipation coefficient DIS4 corresponds to $\text{DIS4} = 0.01, 0.02$, and 0.04 , respectively; low, medium, and high smoothing parameter SMOO corresponds to $\text{SMOO} = 1.0, 0.5$, and 0.0 , respectively. Note that the previous simulations used a “high” value of the numerical dissipation coefficient DIS4 and smoothing parameter SMOO. The figure shows that there is no clear trend for the number of secondary vortices as numerical dissipation is varied. With both parameters, increasing from low to medium values of numerical dissipation causes the number of secondary vortices to increase for most axial stations. However, when increasing from medium to high numerical dissipation, the number of secondary vortices decreases for $x/R \leq 0.4$. When the numerical dissipation parameters are assigned different values, this changes the set of equations that are solved. Therefore, this analysis shows that careful attention should be applied when selecting numerical dissipation inputs since it can have an impact on the resulting wake breakdown, regardless of the subiteration convergence level.

Rotating blade case: Effect of the torus and off-body grid resolution

In this section, the focus is shifted to seeing how grid resolution affects the development of the secondary vortices. As a reminder, the previous simulations in this paper used a torus azimuth resolution of $\Delta\Psi = 0.2^\circ$

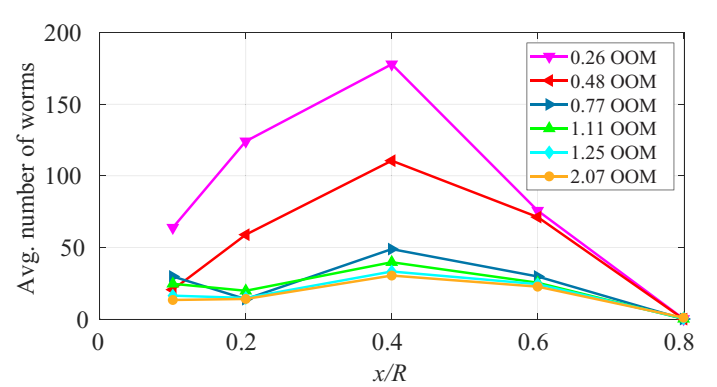


Fig. 22. Average number of secondary vortices per time-step along the downstream distance using 2, 3, 5, 15, 25, and 100 OVERFLOW subiterations, which corresponds to a subiteration residual drop between 0.26 and 2.07 OOM.

and an off-body resolution of $\Delta x = 0.05C_{\text{tip}}$. Figure 26 shows the effect of torus azimuthal (left two columns) and off-body SAMCART (right two columns) resolution on the development of secondary vortices. Azimuth resolution is decreased from $\Delta\Psi = 0.2^\circ$ to $\Delta\Psi = 1.0^\circ$ at a constant off-body spacing of $\Delta x = 0.05C_{\text{tip}}$, and off-body resolution is decreased from $\Delta x = 0.05C_{\text{tip}}$ to $\Delta x = 0.10C_{\text{tip}}$ at a constant torus spacing of $\Delta\Psi = 1.0^\circ$. All simulations are with $\text{SMOO} = 1.0$,

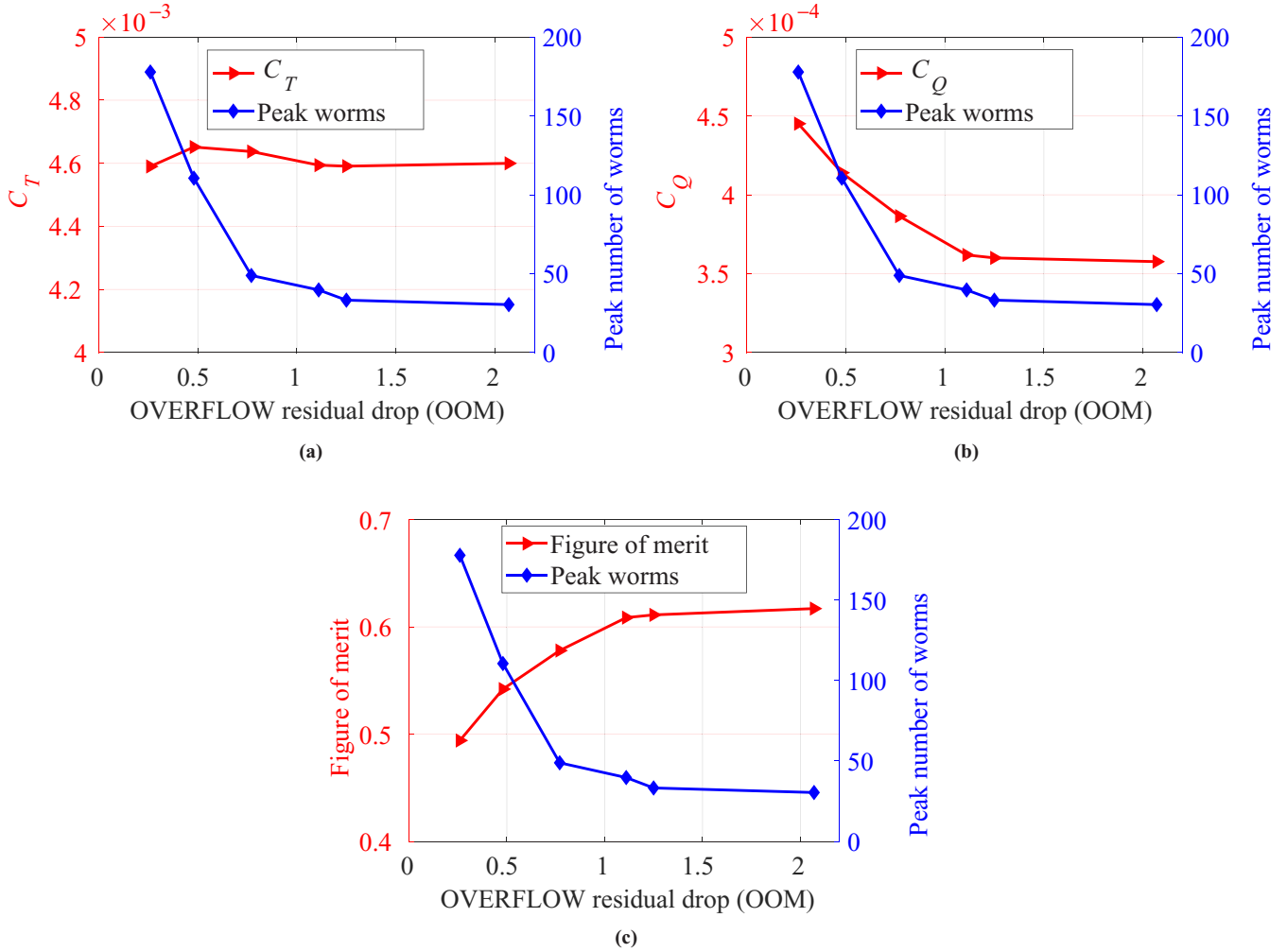


Fig. 23. Comparison of the peak number of secondary vortices (occurring at $x/R = 0.4$) and rotor performance data as the OVERFLOW subiteration residual drop increases.

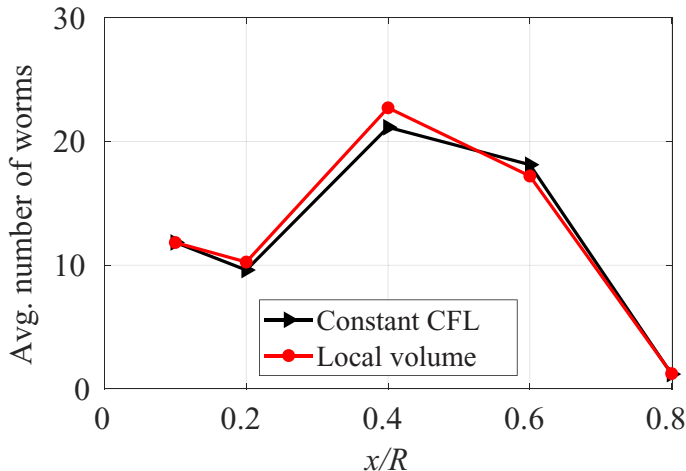


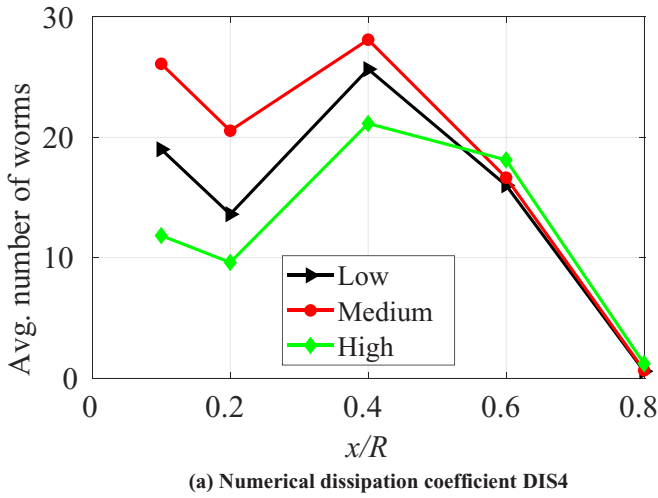
Fig. 24. Comparison of the average number of secondary vortices per time-step along the downstream distance using a constant CFL and heuristic local time-step scaling based on the local volume. Both cases have a subiteration convergence greater than 1.4 OOM for all time steps.

DIS4 = 0.01, and a heuristic local time-step scaling based on the local volume. The OVERFLOW global subiteration residual drop for all simulations is about 0.66 OOM, and the absolute residual is at least 4 OOM. The SAMCART subiteration residual drop for all simulations is about 1.2 OOM. For brevity, only the stationary torus case is shown.

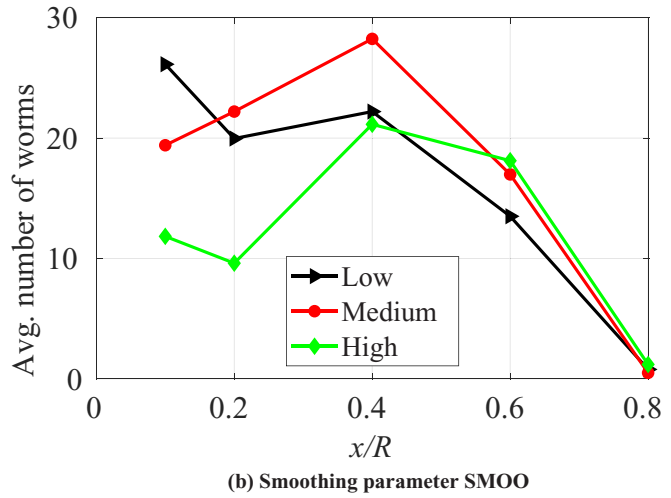
Similar to the previous cases, both the coarser torus and off-body resolution results in fewer secondary vortices wrapping around the first primary vortex and prevents the vortex sheet from attaching to the first primary vortex. These detrimental effects cause fewer secondary vortices to form. The results shown here further support the idea that to accurately predict the secondary vortices not only does the primary vortex structure need to be accurately captured but so does the vortex sheet.

Conclusions and Future Work

In hovering rotor CFD simulations, a common phenomenon is the breakdown of the primary vortex system due to secondary vortices. Since the presence of secondary vortices is strongly influenced by the numerical settings, the degree to which secondary vortices physically occur warrants investigation. Therefore, this study investigated how the numerical settings affect the development of secondary vortices in hover simulations using the rotating blade geometry from previous experiments, where the



(a) Numerical dissipation coefficient DIS4



(b) Smoothing parameter SMOO

Fig. 25. Variation in an average number of secondary vortices per time step as numerical dissipation is varied by changing (a) numerical dissipation coefficient DIS4 and (b) smoothing parameter SMOO. All cases have a subiteration convergence greater than 1.4 OOM for all time-steps. Low, medium, and high numerical dissipation coefficient DIS4 corresponds to $\text{DIS4} = 0.01, 0.02$, and 0.04 , respectively; low, medium, and high smoothing parameter SMOO corresponds to $\text{SMOO} = 1.0, 0.5$, and 0.0 , respectively.

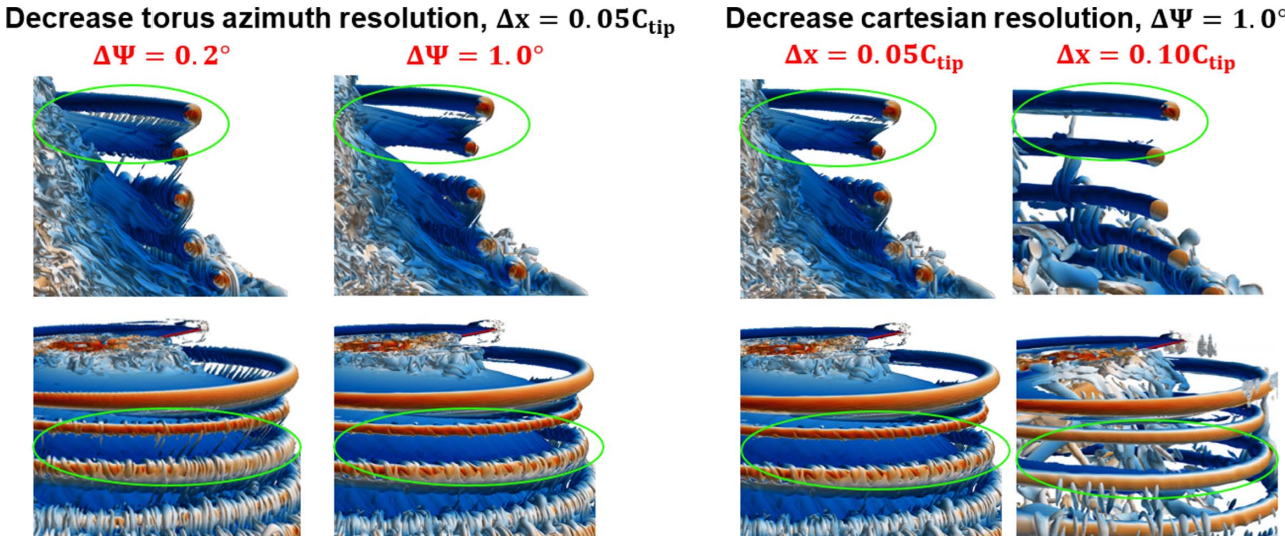


Fig. 26. Full- and cross-sectional view showing the effect of torus azimuthal (left two columns) and off-body SAMCART (right two columns) resolution on the development of secondary vortices. Azimuth resolution is decreased from $\Delta\Psi = 0.2^\circ$ to $\Delta\Psi = 1.0^\circ$. Off-body resolution is decreased from $\Delta x = 0.05C_{\text{tip}}$ to $\Delta x = 0.10C_{\text{tip}}$.

focus is on temporal convergence. A separate vortex ring study was done to better understand how vortex breakdown is influenced by off-body grid structure and different levels of subiteration convergence. The main conclusions drawn from this work are as follows:

1) The Q-criteria isosurfaces from the experiment and simulations had several similarities such as a mix of positive and negative secondary vortices, the width of the vortices, and the evolution of the vortices over time.

2) The secondary vortices develop in the following steps:

a) The vortex sheet shed from the blade wraps around the nearby primary vortex.

b) When it wraps around the primary vortex, it breaks apart into small coherent structures.

c) As the vortex sheet wraps around the nearby primary vortex, it convects downwards towards the next primary vortex.

d) The vortex sheet is entrained into the next primary vortex, which causes the vortex sheet to break apart into elongated s-shaped coherent structures, which are termed “worms.”

3) For relatively high flow solver subiteration convergence, the off-body grid structure and grid rotation has little effect on the development of the secondary vortex structures. However, at low solver subiteration convergence, larger differences occur between the torus and no torus grid structures.

4) A parametric sweep on subiterations shows that as the subiteration residual drop increases the vortex sheet is broken down less, and, correspondingly, both the rotor performance data and peak number of secondary vortices converge.

5) When the subiteration convergence or grid resolution is not high enough, the vortex sheet and primary vortex are broken down, which disrupts the development process and leads to fewer secondary vortices.

6) The vortex ring case showed that when all flow solvers are sufficiently converged, vortex breakdown is minimized, and the solution to the rotating and stationary torus is identical.

7) While the recommended subiteration residual drop appears to depend on the particular solver, it is generally recommended that to ensure the wake is fully converged, the subiterations on all solvers are increased until the number of secondary vortices no longer changes. The recommended grid resolution will depend on resolving the physical vortex sheet thickness and primary vortex core.

Changes in thrust and blade number change the tip vortex separation distance in the helical wake. Therefore, in future work, the effect of thrust and blade number variations on the development of the secondary vortices will be investigated.

Acknowledgments

Discussion with Dr. Christian Wolf from DLR is gratefully acknowledged. DLR also provided the helicopter geometry and experimental data. Feedback from members of the Computational Aeromechanics Group in the U.S. Army Combat Capabilities Development Command Aviation & Missile Center is also appreciated. The material presented in this paper is a product of the CREATE™-AV Element of the Computational Research and Engineering for Acquisition Tools and Environments (CREATE) Program sponsored by the U.S. Department of Defense (DoD) HPC Modernization Program Office. Computational resources provided by the DoD High-Performance Computing Modernization Office, Army S/AAA Roger Strawn, are greatly appreciated.

References

- ¹Abras, J., Hariharan, N. S., and Narducci, R. P., "Wake Breakdown of High fidelity Simulations of a Rotor in Hover," AIAA 2019-0593, Proceedings of the AIAA SciTech 57th Aerospace Sciences Meeting, San Diego, CA, January 7–11, 2019.
- ²Jain, R., "Sensitivity Study of High Fidelity Hover Predictions on the Sikorsky S-76 Rotor," *Journal of Aircraft*, Vol. 55, (1), January 2017, pp. 78–88. DOI: 10.2514/1.C034076.
- ³Jain, R., "A Comparison of CFD Hover Predictions for the Sikorsky S-76 Rotor," AIAA 2016-0032, Proceedings of the AIAA SciTech 54th Aerospace Sciences Meeting, San Diego, CA, January 4–8, 2016.
- ⁴Chaderjian, N., and Buning, P., "High Resolution Navier–Stokes Simulation of Rotor Wakes," Proceedings of the 67th Annual Forum of the American Helicopter Society, Virginia Beach, VA, May 3–5, 2011.
- ⁵Wolf, C. C., Schwarz, C., Kaufmann, K., Gardner, A. D., Michaelis, D., Bosbach, J., Schanz, D., and Schröder, A., "Experimental Study of Secondary Vortex Structures in a Rotor Wake," *Experiments in Fluids*, **60**, 175 (2019). DOI: 10.1007/s00348-019-2807-1.
- ⁶Schanz, D., Gesemann, S., and Schröder, A., "Shake-The-Box: Lagrangian Particle Tracking at High Particle Image Densities," *Experiments in Fluids*, **57**, 70 (2016). DOI: 10.1007/S00348-016-2157-1.
- ⁷Hariharan, N. S., Abras, J., and Narducci, R. P., "An Overview of Wake Breakdown in High-Fidelity Simulations of Rotor-in-Hover," Proceedings of the 67th Annual Forum of the American Helicopter Society, Virginia Beach, VA, October 6–8, 2020.
- ⁸Olsen, J. H., Goldburg, A., and Rogers, M., "Aircraft Wake Turbulence and Its Detection," Proceedings of a Symposium on Aircraft Wake Turbulence, Seattle, WA, September 1–3, 1970.
- ⁹Abras, J., Narducci, R. P., and Hariharan, N. S., "Impact of High-Fidelity Simulation Variations on Wake Breakdown of a Rotor in Hover," AIAA 2020-0531, Proceedings of the AIAA SciTech 58th Aerospace Sciences Meeting, Orlando, FL, January 6–10, 2020.
- ¹⁰Abras, J., and Hariharan, N. S., "Direct Volume Visualization for Deeper Insights on the Physics of 3D Vorticity Dynamics in the Wake of a Hovering Rotor," AIAA 2021-0734, Proceedings of the AIAA Scitech 2021 Forum, Virtual Event, January 11–15 and 19–21, 2021. DOI: 10.2514/6.2021-0734.
- ¹¹Abras, J., and Hariharan, N. S., "Investigation of the Impact of Deep Convergence on Numerical Wake Breakdown of Hovering Rotors," AIAA 2021-0735, Proceedings of the AIAA Scitech 2021 Forum, Virtual Event, January 11–15 and 19–21, 2021. DOI: 10.2514/6.2021-0735.
- ¹²Wissink, A. M., Staruk, W. J., Tran, S. A., Roget, B., Lakshminarayan, V. K., Sitaraman, J., and Jayaraman, B., "Overview of New Capabilities in Helios Version 9.0," AIAA 2019-0839, Proceedings of the 57th AIAA Science and Technology Forum, San Diego, CA, January 7–11, 2019.
- ¹³Sitaraman, J., Floros, M. W., Wissink, A. M., and Potsdam, M., "Parallel Domain Connectivity Algorithm for Unsteady Flow Computations Using Overlapping and Adaptive Grids," *Journal of Computational Physics*, Vol. 229, (12), June 20, 2010, pp. 4703–4723. DOI: 10.1016/j.jcp.2010.03.008.
- ¹⁴Biedron, R. T., Carlson, J., Derlaga, J. M., Gnoffo, P. A., Hammond, D. P., Jones, W. T., Kleb, B., Lee-Rausch, E. M., Nielsen, E., Park, M., Rumsey, C., Thomas, J., Thompson, K. B., and Wood, W., "FUN3D Manual: 13.5," NASA TM 220271, April 2019.
- ¹⁵Allmaras, S. R., Johnson, F., and Spalart, P. R., "Modifications and Clarifications for the Implementation of the Spalart-Allmaras Turbulence Model," Proceedings of the Seventh International Conference on Computational Fluid Dynamics, Big Island, HI, July 2012.
- ¹⁶Dacles-Mariani, J., Kwak, D., and Zilliac, G., "On Numerical Errors and Turbulence Modeling in Tip Vortex Flow Prediction," *International Journal for Numerical Methods in Fluids*, Vol. 30, (1), 1999, pp. 65–82. DOI: 10.1002/(SICI)1097-0363.
- ¹⁷Spalart, P. R., Deck, S., Shur, M. L., Squires, K., Strelets, M. K., and Travin, A., "A New Version of Detached-eddy Simulation, Resistant to Ambiguous Grid Densities," *Theoretical and Computational Fluid Dynamics*, Vol. 20, 2006, pp. 181. DOI: 10.1007/s00162-006-0015-0.
- ¹⁸Buning, P., and Nichols, R., "User's Manual for OVERFLOW 2.3," available at <https://overflow.larc.nasa.gov/users-manual-for-overflow-2-3/>, February 2021.
- ¹⁹Jespersen, D. C., Pulliam, T. H., and Buning, P., "Recent Enhancements to OVERFLOW," AIAA 97-0644, Proceedings of the 35th AIAA Aerospace Sciences Meeting, Reno, NV, January 6–9, 1997.
- ²⁰Shur, M., Stelets, M., Travin, A., and Spalart, P., "Turbulence Modeling in Rotating and Curved Channels: Assessing the Spalart–Shur Correction," *AIAA Journal*, Vol. 38, (5), 2000, pp. 784–792. DOI: 10.2514/2.1058.
- ²¹Wissink, A. M., Sitaraman, J., Jayaraman, B., Roget, B., Lakshminarayan, V. K., Potsdam, M. A., Jain, R., Bauer, A., and Strawn, R., "Recent Advancements in the Helios Rotorcraft Simulation Code," AIAA 2016-0563, Proceedings of the 54th AIAA Aerospace Sciences Meeting, San Diego, CA, January 4–8, 2016.
- ²²Leffell, J. I., Sitaraman, J., Lakshminarayan, V. K., and Wissink, A. M., "Towards Efficient Parallel-in-Time Simulation of Periodic Flows," AIAA 2016-0066, Proceedings of the 54th AIAA Aerospace Sciences Meeting, San Diego, CA, January 4–8, 2016.
- ²³Wissink, A. M., Jayaraman, B., Tran, S. A., Jain, R., Potsdam, M. A., Sitaraman, J., Roget, B., and Lakshminarayan, V. K., "Assessment of Rotorcraft Download Using Helios v8," AIAA 2018-0026, Proceedings of the 2018 AIAA Aerospace Sciences Meeting, Kissimmee, FL, January 8–12, 2018.

²⁴Yoon, S., Pulliam, T. H., and Chaderjian, N. M., "Simulations of XV-15 Rotor Flows in Hover Using OVERFLOW," Proceedings of the 50th AHS Aeromechanics Specialists, AHS, San Francisco, CA, January 22-24, 2014, pp. 1-11.

²⁵Gibeau, B., Koch, C., and Ghaemi, S., "Secondary Instabilities in the Wake of an Elongated Two-dimensional Body with a Blunt Trailing Edge," *Journal of Fluid Mechanics*, Vol. 846, July 2018, pp. 578-604. DOI: 10.1017/jfm.2018.285.

²⁶Jain, R., and Conlisk, A. T., "Interaction of Tip-Vortices in the Wake of a Two-Bladed Rotor in Axial Flight," *Journal of the American Helicopter Society*, Vol. 45, (3), July 2000, pp. 157-164. DOI: 10.4050/JAHS.45.157.

²⁷Sherer, S. E., and Visbal, M. R., "Multi-resolution Implicit Large Eddy Simulations using a High-order Overset-grid Approach," *International Journal for Numerical Methods in Fluids*, Vol. 55, (5), 2007, pp. 455-482. DOI: 10.1002/fld.1463.

²⁸Schwarz, C., Bodling, A., Wolf, C. C., Brinkema, R., Potsdam, M., and Gardner, A. D., "Development of Secondary Vortex Structures in Rotor Wakes," *Experiments in Fluids*, **63**, (2021). DOI: 10.1007/s00348-021-03348-8.

²⁹Chen, Q., Zhong, Q., Qi, M., and Wang, X., "Comparison of Vortex Identification Criteria for Planar Velocity Fields in Wall Turbulence," *Physics of Fluids*, **27** (8), 085101 (2015). DOI: 10.1063/1.4927647.